



Output-only identification of self-excited systems using discrete-time Lur'e models with application to a gas-turbine combustor

Juan A. Paredes, Yulong Yang & Dennis S. Bernstein

To cite this article: Juan A. Paredes, Yulong Yang & Dennis S. Bernstein (2022): Output-only identification of self-excited systems using discrete-time Lur'e models with application to a gas-turbine combustor, International Journal of Control, DOI: [10.1080/00207179.2022.2137702](https://doi.org/10.1080/00207179.2022.2137702)

To link to this article: <https://doi.org/10.1080/00207179.2022.2137702>



Published online: 02 Nov 2022.



Submit your article to this journal [↗](#)



Article views: 12



View related articles [↗](#)



View Crossmark data [↗](#)



Output-only identification of self-excited systems using discrete-time Lur'e models with application to a gas-turbine combustor

Juan A. Paredes , Yulong Yang and Dennis S. Bernstein 

Department of Aerospace Engineering, University of Michigan, Ann Arbor, MI, USA

ABSTRACT

A self-excited system is a nonlinear system with the property that a constant input yields a bounded, non-convergent response. Nonlinear identification of self-excited systems is considered using a Lur'e model structure, where a linear model is connected in feedback with a nonlinear feedback function. To facilitate identification, the nonlinear feedback function is assumed to be continuous and piecewise affine (CPA). The present paper uses least-squares optimisation to estimate the coefficients of the linear dynamics and the slope vector of the CPA nonlinearity, as well as mixed-integer optimisation to estimate the order of the linear dynamics and the breakpoints of the CPA function. The proposed identification technique requires only output data, and thus no measurement of the constant input is required. This technique is illustrated on a diverse collection of low-dimensional numerical examples as well as data from a gas-turbine combustor.

ARTICLE HISTORY

Received 4 May 2022
Accepted 9 October 2022

KEYWORDS

Nonlinear system identification; nonlinear feedback; self-excited oscillations; least squares; mixed-integer optimisation

1. Introduction

A self-excited system (SES) has the property that its response to a constant input is bounded and nonconvergent. Although an undamped oscillator as well as some linear systems with time delay are self-excited, these systems lack structural robustness in the sense that arbitrarily small perturbations of the dynamics can lead to either a convergent (damped) or divergent (unbounded) response. Structurally robust SES's are thus nonlinear. The classical example of an SES is the second-order van der Pol oscillator, for which all trajectories except for the zero equilibrium converge to a limit cycle. An SES, however, need not possess a limit cycle.

Self-excited systems arise in surprisingly diverse applications. Specific examples can be found in chemical and biochemical systems (Goldbeter & Berridge, 1996; Gray & Scott, 1990), fluid-structure interaction (Blevins, 1990; Gianikos et al., 2020; Jonsson et al., 2019), and thermoacoustic oscillation (Chen & Driscoll, 2016; Dowling, 1997). Overviews of SES are given in Jenkins (2013) and Ding (2010).

In view of these diverse applications, it is of interest to construct models of SES based on response data. To this end, a candidate model structure is the Lur'e model, where linear dynamics are connected in feedback with a static nonlinear function (Khalil, 2002). The ability of Lur'e models to exhibit self-oscillation has been widely studied (Aguilar et al., 2009; Chatterjee, 2011; Ding, 2010; Mees & Chua, 1979; Risau-Gusman, 2016; Stan & Sepulchre, 2007; Zanette, 2017), and self-excited discrete-time systems are considered in Rasvan (1998), D'Amico et al. (2002), Gentile et al. (2011). As shown in Paredes et al. (2021), a Lur'e model exhibits self-excited behaviour when the linear dynamics are asymptotically stable, the nonlinear feedback function is sigmoidal, and the loop gain is sufficiently

high. In effect, high loop gain renders the zero equilibrium unstable, driving the state to the saturation region, where the system operates as an open-loop system driven by a step input. A washout filter (an asymptotically stable transfer function with a zero at 1 and thus zero asymptotic step response) drives the state of the open-loop asymptotically stable dynamics back into the linear region, which yields an oscillatory response.

The present paper applies nonlinear system identification to construct a Lur'e model for SES. This approach does not assume or require that the SES possess a Lur'e structure; rather, the goal is to estimate a linear model G and a nonlinear feedback function ϕ that, when combined into a Lur'e model, capture the nonconvergent behaviour of the SES. For example, although the van der Pol oscillator is a Lur'e model with a 2-input, 1-output nonlinear feedback function, the present paper uses a Lur'e model with a 1-input, 1-output nonlinear feedback function for system identification.

For nonlinear system identification, the present paper applies a variation of the technique in Van Pelt and Bernstein (2001). As in Van Pelt and Bernstein (2001), the nonlinear feedback function is parameterised as a continuous, piecewise-affine (CPA) function, where the slope of each segment is estimated for a given partition of the domain of the CPA function. Although the domain of ϕ is known from data, the number and locations of the breakpoints of the CPA function were determined in Paredes and Bernstein (2021) by trial and error. The contribution of the present paper is to use mixed-integer optimisation to automate and optimise a subset of the parameters needed for the identified Lur'e model, while using least-squares optimisation to estimate the remaining parameters. By encompassing both continuous and discrete variables, the present paper shows that mixed integer optimisation (Belotti et al., 2013; Floudas, 1995)

is advantageous for identifying Lur'e models with a CPA nonlinear feedback function. Mixed integer optimisation has been used for system identification in Roll et al. (2004), Dua (2010), Förster et al. (2019) and Mejari et al. (2020).

Since the objective of this paper is to identify self-excited systems, the input is assumed to be constant. However, the approach of the present paper does not require knowledge of the constant input, and thus measurements of only the output are needed. Numerical examples show that measurements of the self-excited response of the system, including the transient and asymptotic response for systems that are asymptotically periodic, is sufficient for identifying a Lur'e model that reproduces the asymptotic waveform and, in many cases, the shape of the nonlinearity as well.

The contents of this paper are as follows. Section 2 introduces the discrete-time Lur'e (DTL) system and the conditions under which a DTL system is a SES. Section 3 introduces the filtered time-delayed DTL (FTDDTL) system as a special case of the DTL system. Section 4 introduces the discrete-time Lur'e identification (DTLI) model, which has the form of the FTDDTL, as well as the parameterisation of the CPA function used to approximate the nonlinear feedback function. Section 5 presents the nonlinear least-squares technique used for identifying SES using the DTLI model, which is an modification of the technique presented in Paredes and Bernstein (2021). Section 6 presents the mixed-integer optimisation framework used in this paper for identifying SES using the DTLI model. Section 7 presents numerical examples in which FTDDTL systems are identified using DTLI models. Section 8 presents numerical examples in which the logistic map DTL system under various parameters is identified using DTLI models. Section 9 presents the continuous-time Lur'e (CTL) system, and Section 10 presents numerical examples in which continuous-time systems are identified using DTLI models. Section 11 presents the results obtained from applying the proposed identification technique on experimental data obtained from a flute and a gas-turbine combustor. Finally, Section 12 presents conclusions and future work.

Notation. $\mathbb{R} \triangleq (-\infty, \infty)$ and $\mathbb{N}_0 \triangleq \{0, 1, 2, \dots\}$. For $x \in \mathbb{R}^n$, $\|x\|_2$ is the Euclidean norm of x . For $A \in \mathbb{R}^{n \times m}$, $\text{vec } A \in \mathbb{R}^{nm}$ is the vector formed by stacking the columns of A , vec^{-1} satisfies $A = \text{vec}^{-1}(\text{vec } A)$, $\|A\|_F$ is the Frobenius norm of A , and $\sigma_{\max}(A)$ is the largest singular value of A . $1_{n \times m} \in \mathbb{R}^{n \times m}$ is a matrix whose entries are all ones.

2. Discrete-time Lur'e system

We consider the *discrete-time Lur'e* (DTL) system shown in Figure 1, which has the dynamics

$$x_{k+1} = Ax_k + Bu_k + Dv_k, \quad (1)$$

$$y_k = Cx_k. \quad (2)$$

$$z_k = Ex_k, \quad (3)$$

$$u_k = \phi(z_k), \quad (4)$$

where $k \in \mathbb{N}_0$, $x_k \in \mathbb{R}^n$, $u_k \in \mathbb{R}^m$, $v_k \in \mathbb{R}$, $y_k \in \mathbb{R}$, $z_k \in \mathbb{R}^p$, $A \in \mathbb{R}^{n \times n}$, $B \in \mathbb{R}^{n \times m}$, $C \in \mathbb{R}^{1 \times n}$, $D \in \mathbb{R}^{n \times 1}$, $E \in \mathbb{R}^{p \times n}$, and ϕ :

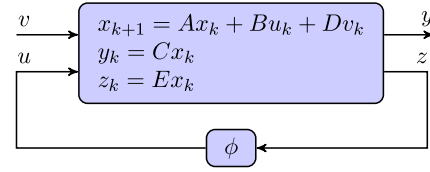


Figure 1. Discrete-time Lur'e system with constant input v , output y , and nonlinear feedback function ϕ .

$\mathbb{R}^p \rightarrow \mathbb{R}^m$. Combining (1)–(4) yields

$$x_{k+1} = Ax_k + B\phi(Ex_k) + Dv_k, \quad (5)$$

$$y_k = Cx_k. \quad (6)$$

As illustrated by the following examples, many nonlinear discrete-time systems can be written in the form of (5), (6).

Example 2.1: The dynamics of the logistic map are given by

$$x_{k+1} = \gamma x_k - \gamma \phi(x_k), \quad (7)$$

$$y_k = z_k = x_k, \quad (8)$$

$$\phi(x_k) = x_k^2, \quad (9)$$

where $n = m = p = 1$ and $x_k, y_k, z_k, \gamma \in \mathbb{R}$.

Example 2.2: The dynamics of the density-dependent Leslie matrix with two age classes (equation 4.1 of Guckenheimer et al., 1977) are given by

$$x_{k+1} = \begin{bmatrix} 0 & 0 \\ \gamma & 0 \end{bmatrix} x_k + \begin{bmatrix} 1 \\ 0 \end{bmatrix} \phi(x_k), \quad (10)$$

$$y_k = \begin{bmatrix} 0 & 1 \end{bmatrix} x_k, \quad (11)$$

$$\phi(x_k) = (\xi_1 x_{1,k} + \xi_2 x_{2,k}) e^{-\alpha(x_{1,k} + x_{2,k})}, \quad (12)$$

where $n = p = 2$, $m = 1$, $z_k = x_k = [x_{1,k} \ x_{2,k}]^T \in \mathbb{R}^2$, $y_k \in \mathbb{R}$, and $\alpha, \gamma, \xi_1, \xi_2 \in \mathbb{R}$.

Examples 2.1 and 2.2 exhibit oscillatory responses, thus motivating the following definition.

Definition 2.3: The DTL system (5), (6) is a *self-excited system* (SES) if, for all constant v_k , the following statements hold:

- (i) For all $x_0 \in \mathbb{R}^n$, $(y_k)_{k=1}^\infty$ is bounded.
- (ii) For almost all $x_0 \in \mathbb{R}^n$, $\lim_{k \rightarrow \infty} y_k$ does not exist.

Numerical examples given in Section 8 show that *ii*) in Definition 2.3 may be satisfied when y is asymptotically periodic or chaotic.

3. Filtered time-delayed DTL system

In this section we consider a special case of the DTL system structure. In particular, the *filtered time-delayed DTL* (FTDDTL) system shown in Figure 2 includes a transfer function G , a time delay G_d , a washout filter G_f , and a nonlinear feedback

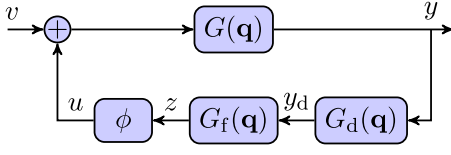


Figure 2. Filtered time-delayed discrete-time Lur'e (FTDDTL) system with input v , asymptotically stable plant $G(\mathbf{q})$, time delay $G_d(\mathbf{q})$, washout filter $G_f(\mathbf{q})$, and nonlinear feedback function ϕ .

function ϕ . Under suitable assumptions, it is shown in Paredes et al. (2020) that this structure gives rises to self-excited oscillations.

The n th-order, asymptotically stable, strictly proper transfer function G has the form

$$G(\mathbf{q}) = \frac{\mathcal{B}(\mathbf{q})}{\mathcal{A}(\mathbf{q})} = \frac{b_1 \mathbf{q}^{-1} + \dots + b_n \mathbf{q}^{-n}}{1 + a_1 \mathbf{q}^{-1} + \dots + a_n \mathbf{q}^{-n}}, \quad (13)$$

where \mathbf{q} is the forward-shift operator (used in place of the Z -transform variable in order to include both the free and forced response), the time delay G_d is given by

$$G_d(\mathbf{q}) = \mathbf{q}^{-d}, \quad (14)$$

where d is a nonnegative integer, the washout filter G_f is given by

$$G_f(\mathbf{q}) = \frac{\mathbf{q} - 1}{\mathbf{q}} = 1 - \mathbf{q}^{-1}, \quad (15)$$

and the nonlinear feedback function $\phi : \mathbb{R} \rightarrow \mathbb{R}$ satisfies

$$u_k = \phi(z_k). \quad (16)$$

Using $y_k = G(\mathbf{q})(u_k + v_k)$, it follows that

$$\mathcal{A}(\mathbf{q})y_k = \mathcal{B}(\mathbf{q})(\phi(z_k)) + v_k, \quad (17)$$

and thus, for all $k \geq n + d + 1$,

$$\begin{aligned} y_k &= (1 - \mathcal{A}(\mathbf{q}))y_k + \mathcal{B}(\mathbf{q})(\phi(z_k) + v_k) \\ &= -a_1 y_{k-1} - \dots - a_n y_{k-n} + b_1 \phi(z_{k-1}) + \dots \\ &\quad + b_n \phi(z_{k-n}) + b_1 v_{k-1} + \dots + b_n v_{k-n}, \end{aligned} \quad (18)$$

where

$$z_k = y_{k-d} - y_{k-d-1}, \quad (19)$$

with the initial output values y_0, \dots, y_{n+d} . Note that (18), (19) can be written as

$$\begin{aligned} x_{k+1} &= \begin{bmatrix} A_G & 0_{n \times d} & 0_{n \times 1} \\ B_d C_G & A_d & 0_{d \times 1} \\ 0_{1 \times n} & C_d & 0 \end{bmatrix} x_k \\ &\quad + \begin{bmatrix} B_G \\ 0_{(d+1) \times 1} \end{bmatrix} [\phi([0_{1 \times n} \quad C_d \quad -1]x_k) + v_k], \end{aligned} \quad (20)$$

$$y_k = [C_G \quad 0_{1 \times (d+1)}] x_k, \quad (21)$$

where $x_k \in \mathbb{R}^{n+d+1}$, (A_G, B_G, C_G) is a minimal realisation of G , and (A_d, B_d, C_d) is a minimal realisation of G_d . Hence, (20), (21) is special case of (5), (6).

4. Discrete-time Lur'e identification model

To facilitate identification, we consider the *discrete-time Lur'e identification* (DTLI) model, which has the form of the FTD-DTL. The DTLI model, which is shown in Figure 3, incorporates the \hat{n} th-order, asymptotically stable, strictly proper linear dynamics

$$\hat{G}(\mathbf{q}) = \frac{\hat{\mathcal{B}}(\mathbf{q})}{\hat{\mathcal{A}}(\mathbf{q})} = \frac{\hat{b}_1 \mathbf{q}^{-1} + \dots + \hat{b}_{\hat{n}} \mathbf{q}^{-\hat{n}}}{1 + \hat{a}_1 \mathbf{q}^{-1} + \dots + \hat{a}_{\hat{n}} \mathbf{q}^{-\hat{n}}}, \quad (22)$$

the constant input \hat{v} , the time delay

$$\hat{G}_d(\mathbf{q}) = \mathbf{q}^{-\hat{d}}, \quad (23)$$

where \hat{d} is a nonnegative integer, the washout filter G_f given by (15), and the nonlinear feedback function $\hat{\phi} : \mathbb{R} \rightarrow \mathbb{R}$ written as

$$\hat{u}_k = \hat{\phi}(\hat{z}_k). \quad (24)$$

Using $\hat{y}_k = \hat{G}(\mathbf{q})(\hat{u}_k + \hat{v})$, it follows that

$$\hat{\mathcal{A}}(\mathbf{q})\hat{y}_k = \hat{\mathcal{B}}(\mathbf{q})(\hat{\phi}(\hat{z}_k) + \hat{v}), \quad (25)$$

and thus, for all $k \geq \hat{n} + \hat{d} + 1$,

$$\begin{aligned} \hat{y}_k &= (1 - \hat{\mathcal{A}}(\mathbf{q}))\hat{y}_k + \hat{\mathcal{B}}(\mathbf{q})(\hat{\phi}(\hat{z}_k) + \hat{v}) \\ &= -\hat{a}_1 \hat{y}_{k-1} - \dots - \hat{a}_{\hat{n}} \hat{y}_{k-\hat{n}} + \hat{b}_1 \hat{\phi}(\hat{z}_{k-1}) + \dots \\ &\quad + \hat{b}_{\hat{n}} \hat{\phi}(\hat{z}_{k-\hat{n}}) + (\hat{b}_1 + \dots + \hat{b}_{\hat{n}})\hat{v}, \end{aligned} \quad (26)$$

where

$$\hat{z}_k = \hat{y}_{k-\hat{d}} - \hat{y}_{k-\hat{d}-1}. \quad (27)$$

Since \hat{v} is not measured in output-only identification and the input to \hat{G} is $\hat{\phi}(\hat{z}_k) + \hat{v}$, the range space of $\hat{\phi}$ can be shifted arbitrarily. Hence, we assume without loss of generality that $\hat{\phi}(0) = 0$.

For system identification, we use a *continuous, piecewise-affine* (CPA) model $\hat{\phi}$ of ϕ with the following parameterisation. Let $(-\infty, \hat{c}_1], (\hat{c}_1, \hat{c}_2], \dots, (\hat{c}_{\hat{p}-1}, \hat{c}_{\hat{p}}], (\hat{c}_{\hat{p}}, \infty)$ be a partition of the domain \mathbb{R} of $\hat{\phi}$, and define the vector

$$\hat{c} \triangleq [\hat{c}_1 \quad \dots \quad \hat{c}_{\hat{p}}]^T \in \mathbb{R}^{\hat{p}}. \quad (28)$$

Since $\hat{\phi}(0) = 0$, let $\hat{c}_{\hat{r}} = 0$, where $\hat{r} \in [1, \hat{p}]$, and thus $\hat{\phi}(\hat{c}_{\hat{r}}) = \hat{\phi}(0) = 0$. Furthermore, for all $i \in [1, \hat{p} + 1]$, let $\hat{\mu}_i$ denote the

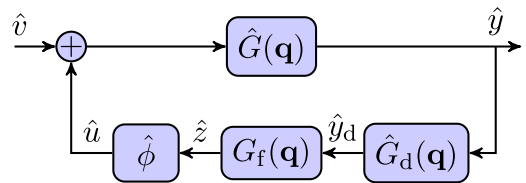


Figure 3. Discrete-time Lur'e identification (DTLI) model with constant input \hat{v} , asymptotically stable plant $\hat{G}(\mathbf{q})$, time delay $\hat{G}_d(\mathbf{q})$, washout filter $G_f(\mathbf{q})$, and nonlinear feedback function $\hat{\phi}$. The structure of the DTLI model coincides with the structure of the FTDDTL system.

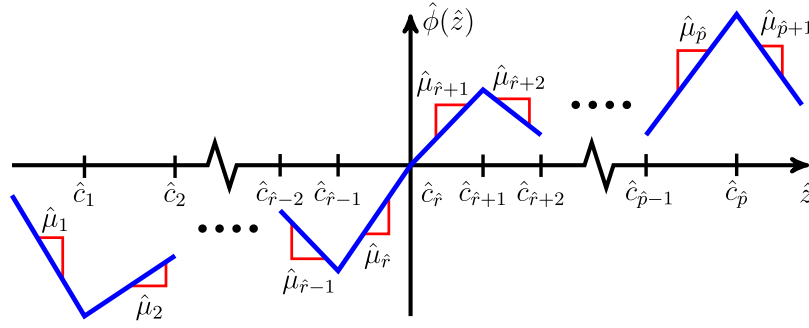


Figure 4. Parameterization of the CPA function $\hat{\phi}$. Note that $\hat{c}_{\hat{r}} = 0$ and $\hat{\phi}(\hat{c}_{\hat{r}}) = \hat{\phi}(0) = 0$.

slope of $\hat{\phi}$ in the i th partition interval, and define the slope vector

$$\hat{\mu} \triangleq [\hat{\mu}_1 \quad \dots \quad \hat{\mu}_{\hat{p}+1}]^T \in \mathbb{R}^{\hat{p}+1}. \quad (29)$$

Then, for all $\hat{z} \in \mathbb{R}$, $\hat{\phi}$ can be written as

$$\hat{\phi}(\hat{z}) = \hat{\mu}^T \hat{\eta}(\hat{z}), \quad (30)$$

where $\hat{\eta} : \mathbb{R} \rightarrow \mathbb{R}^{\hat{p}+1}$ is given by

$$\hat{\eta}(\hat{z}) \triangleq \begin{cases} \hat{\eta}_1(\hat{z}), & \hat{\delta}(\hat{z}) < \hat{r} + 1, \\ \hat{\eta}_2(\hat{z}), & \hat{\delta}(\hat{z}) \geq \hat{r} + 1, \end{cases} \quad (31)$$

$\hat{\delta}(\hat{z}) \in [1, \hat{p} + 1]$ is the index of the partition interval containing \hat{z} , and

$$\hat{\eta}_1(\hat{z}) \triangleq [0_{1 \times (\hat{\delta}(\hat{z})-1)} \quad \hat{z} - \hat{c}_{\hat{\delta}(\hat{z})} \quad \hat{c}_{\hat{\delta}(\hat{z})} - \hat{c}_{\hat{\delta}(\hat{z})+1} \quad \dots \quad \hat{c}_{\hat{r}-1} - \hat{c}_{\hat{r}} \quad 0_{1 \times (\hat{p}+1-\hat{r})}]^T, \quad (32)$$

$$\hat{\eta}_2(\hat{z}) \triangleq [0_{1 \times \hat{r}} \quad \hat{c}_{\hat{r}+1} - \hat{c}_{\hat{r}} \quad \dots \quad \hat{c}_{\hat{\delta}(\hat{z})-1} - \hat{c}_{\hat{\delta}(\hat{z})-2} \quad \hat{z} - \hat{c}_{\hat{\delta}(\hat{z})-1} \quad 0_{1 \times (\hat{p}+1-\hat{\delta}(\hat{z}))}]^T. \quad (33)$$

Figure 4 illustrates the parameterisation of the CPA function $\hat{\phi}$ in terms of \hat{c} , $\hat{\mu}$, and \hat{r} .

Next, consider DTLI/CPA, which is DTLI with CPA $\hat{\phi}$. It thus follows from (26) and (30) that

$$\begin{aligned} \hat{y}_k = & -\hat{a}_1 \hat{y}_{k-1} - \dots - \hat{a}_{\hat{n}} \hat{y}_{k-\hat{n}} + \hat{b}_1 \hat{\mu}^T \hat{\eta}(\hat{z}_{k-1}) + \dots \\ & + \hat{b}_{\hat{n}} \hat{\mu}^T \hat{\eta}(\hat{z}_{k-\hat{n}}) + 1_{1 \times \hat{n}} \hat{b} \hat{v}, \end{aligned} \quad (34)$$

where

$$\hat{a} \triangleq \begin{bmatrix} \hat{a}_1 \\ \vdots \\ \hat{a}_{\hat{n}} \end{bmatrix}, \quad \hat{b} \triangleq \begin{bmatrix} \hat{b}_1 \\ \vdots \\ \hat{b}_{\hat{n}} \end{bmatrix}. \quad (35)$$

Then, (34) can be written as

$$\hat{y}_k = -\hat{\phi}_k^T \hat{a} + \hat{\phi}_{\hat{\eta},k}^T \hat{b} + 1_{1 \times \hat{n}} \hat{b} \hat{v} = \hat{\phi}_k^T \hat{\theta}, \quad (36)$$

where

$$\begin{aligned} \hat{\phi}_k & \triangleq \begin{bmatrix} -\hat{\phi}_{\hat{y},k} \\ \hat{\phi}_{\hat{\eta},k} \\ 1 \end{bmatrix} \in \mathbb{R}^{\hat{n}(\hat{p}+2)+1}, \\ \hat{\theta} & \triangleq \begin{bmatrix} \hat{a} \\ \text{vec}(\hat{\mu} \hat{b}^T) \\ 1_{1 \times \hat{n}} \hat{b} \hat{v} \end{bmatrix} \in \mathbb{R}^{\hat{n}(\hat{p}+2)+1} \end{aligned} \quad (37)$$

$$\begin{aligned} \hat{\phi}_{\hat{y},k} & \triangleq \begin{bmatrix} \hat{y}_{k-1} \\ \vdots \\ \hat{y}_{k-\hat{n}} \end{bmatrix} \in \mathbb{R}^{\hat{n}}, \\ \hat{\phi}_{\hat{\eta},k} & \triangleq \begin{bmatrix} \hat{\eta}(\hat{z}_{k-1}) \\ \vdots \\ \hat{\eta}(\hat{z}_{k-\hat{n}}) \end{bmatrix} \in \mathbb{R}^{\hat{n}(\hat{p}+1)}. \end{aligned} \quad (38)$$

5. Nonlinear least-squares optimisation for system identification

In this section, we use a technique based on least squares to construct a DTLI/CPA model \mathcal{M} that approximates the response of the self-excited system \mathcal{S} . This technique is a variation of the method used in Van Pelt and Bernstein (2001). The objective is to determine a transfer function \hat{G} , delay \hat{d} , and CPA function $\hat{\phi}$ such that the response of the identified model \mathcal{M} approximates the response of \mathcal{S} . This technique requires a choice of $\hat{n}, \hat{d}, \hat{c}, \hat{r}$; these values are then used to obtain parameter estimates $\hat{a}, \hat{b}, \hat{v}, \hat{\mu}$. In the next section, an optimisation technique is used to update the parameter estimates $\hat{n}, \hat{d}, \hat{c}, \hat{r}$. In the special case where \mathcal{S} is a FTDDTL system with CPA function ϕ , the parameters $\hat{n}, \hat{d}, \hat{c}, \hat{r}, \hat{a}, \hat{b}, \hat{v}, \hat{\mu}$ are estimates of n, d, c, r, a, b, v, μ .

For system identification, we use measurements of y from a data window, which may include portions of the transient and asymptotic response. To define the data window, let $l_u \geq l_l \geq \hat{n} + \hat{d} + 1$, and assume that measurements of y_k are available for all $k \in [l_l - \hat{n} - \hat{d} - 1, l_u]$. The objective is to minimise a cost function involving, for all $k \in [l_l, l_u]$, the difference $y_k - \hat{y}_k$ between the measurement y_k from \mathcal{S} and the output \hat{y}_k of the DTLI/CPA model \mathcal{M} , where \hat{y}_k is obtained by propagating (34), where, for all $\kappa \in [k - \hat{d} - \hat{n} - 1, k - 1]$, the initial values are given by $\hat{y}_\kappa = y_\kappa$. Hence, we define the least-squares cost

$$J(\hat{a}, \hat{b}, \hat{v}, \hat{\mu}) \triangleq \|Y - \Phi \hat{\theta}\|_2, \quad (39)$$

where $\hat{\theta}$ is defined by (37),

$$Y \triangleq \begin{bmatrix} y_{l_l} \\ \vdots \\ y_{l_u} \end{bmatrix} \in \mathbb{R}^{l_u - l_l + 1} \quad (40)$$

and

$$\Phi \triangleq [-\Phi_y \quad \Phi_{\hat{\eta}} \quad \mathbf{1}_{(l_u-l+1) \times 1}] \in \mathbb{R}^{(l_u-l+1) \times (\hat{n}(\hat{p}+2)+1)}, \quad (41)$$

where

$$\begin{aligned} \Phi_y &\triangleq \begin{bmatrix} \varphi_{y,l_1} \\ \vdots \\ \varphi_{y,l_u} \end{bmatrix} \in \mathbb{R}^{(l_u-l+1) \times \hat{n}}, \\ \Phi_{\hat{\eta}} &\triangleq \begin{bmatrix} \varphi_{\hat{\eta},l_1} \\ \vdots \\ \varphi_{\hat{\eta},l_u} \end{bmatrix} \in \mathbb{R}^{(l_u-l+1) \times (\hat{n}(\hat{p}+1))}, \end{aligned} \quad (42)$$

and, for all $k \in [l, l_u]$,

$$\varphi_{y,k} \triangleq [y_{k-1} \quad \cdots \quad y_{k-\hat{n}}] \in \mathbb{R}^{1 \times \hat{n}}, \quad (43)$$

$$\begin{aligned} \varphi_{\hat{\eta},k} &\triangleq [\hat{\eta}(y_{k-\hat{d}-1} - y_{k-\hat{d}-2}) \quad \cdots \quad \hat{\eta}(y_{k-\hat{d}-\hat{n}} - y_{k-\hat{d}-\hat{n}-1})] \\ &\in \mathbb{R}^{1 \times (\hat{n}(\hat{p}+1))}. \end{aligned} \quad (44)$$

Since $\hat{\theta}$ defined by (37) is a nonlinear function of $\hat{b}, \hat{v}, \hat{\mu}$, we derive an upper bound for J , which is subsequently minimised by means of a two-step process. To do this, let $\hat{\theta}_{\hat{\mu}} \in \mathbb{R}^{\hat{n}(\hat{p}+1)}$ be an approximation of $\text{vec}(\hat{\mu}\hat{b}^T)$ and define

$$\hat{\theta}_{\hat{v}} \triangleq \mathbf{1}_{1 \times \hat{n}} \hat{b} \hat{v} \in \mathbb{R}, \quad (45)$$

$$\tilde{\theta} \triangleq \begin{bmatrix} \hat{a} \\ \hat{\theta}_{\hat{\mu}} \\ \hat{\theta}_{\hat{v}} \end{bmatrix} \in \mathbb{R}^{\hat{n}(\hat{p}+2)+1}, \quad (46)$$

and the cost functions

$$J_1(\tilde{\theta}) \triangleq \|Y - \Phi\tilde{\theta}\|_2, \quad (47)$$

$$J_2(\hat{\theta}_{\hat{\mu}}, \hat{\mu}, \hat{b}) \triangleq \|\hat{\theta}_{\hat{\mu}} - \text{vec}(\hat{\mu}\hat{b}^T)\|_2. \quad (48)$$

Proposition 5.1: Let $\hat{\theta}_{\hat{\mu}} \in \mathbb{R}^{\hat{n}(\hat{p}+1)}$, define $\tilde{\theta}$ by (46), and define J, J_1 , and J_2 by (39), (47), and (48). Then,

$$J(\hat{a}, \hat{b}, \hat{v}, \hat{\mu}) \leq J_1(\tilde{\theta}) + \sigma_{\max}(\Phi_{\hat{\eta}})J_2(\hat{\theta}_{\hat{\mu}}, \hat{\mu}, \hat{b}). \quad (49)$$

Proof: Note that (39) can be written as

$$\begin{aligned} J(\hat{a}, \hat{b}, \hat{v}, \hat{\mu}) &= \|Y - \Phi\hat{\theta} + \Phi_{\hat{\eta}}\hat{\theta}_{\hat{\mu}} - \Phi_{\hat{\eta}}\hat{\theta}_{\hat{\mu}}\|_2 \\ &= \|Y + \Phi_y\hat{a} - \Phi_{\hat{\eta}}\text{vec}(\hat{\mu}\hat{b}^T) \\ &\quad - \mathbf{1}_{(l_u-l+1) \times 1}\hat{\theta}_{\hat{v}} + \Phi_{\hat{\eta}}\hat{\theta}_{\hat{\mu}} - \Phi_{\hat{\eta}}\hat{\theta}_{\hat{\mu}}\|_2 \\ &= \|Y - \Phi\tilde{\theta} + \Phi_{\hat{\eta}}(\hat{\theta}_{\hat{\mu}} - \text{vec}(\hat{\mu}\hat{b}^T))\|_2, \end{aligned}$$

which implies that

$$\begin{aligned} J(\hat{a}, \hat{b}, \hat{v}, \hat{\mu}) &\leq \|Y - \Phi\tilde{\theta}\|_2 + \|\Phi_{\hat{\eta}}(\hat{\theta}_{\hat{\mu}} - \text{vec}(\hat{\mu}\hat{b}^T))\|_2 \\ &\leq \|Y - \Phi\tilde{\theta}\|_2 + \sigma_{\max}(\Phi_{\hat{\eta}})\|\hat{\theta}_{\hat{\mu}} - \text{vec}(\hat{\mu}\hat{b}^T)\|_2 \\ &= J_1(\tilde{\theta}) + \sigma_{\max}(\Phi_{\hat{\eta}})J_2(\hat{\theta}_{\hat{\mu}}, \hat{\mu}, \hat{b}). \quad \blacksquare \end{aligned}$$

The upper bound for J given by (49) is minimised by sequentially minimising J_1 and J_2 . First, J_1 is minimised to obtain $\tilde{\theta}$, such that

$$\tilde{\theta} = \begin{bmatrix} \hat{a} \\ \hat{\theta}_{\hat{\mu}} \\ \hat{\theta}_{\hat{v}} \end{bmatrix} = \underset{\tilde{\theta} \in \mathbb{R}^{\hat{n}(\hat{p}+2)+1}}{\text{argmin}} J_1(\tilde{\theta}). \quad (50)$$

Since J_1 is a linear least-squares function of $\tilde{\theta}$, we use *recursive least squares* (RLS) (Aström & Wittenmark, 1995) with $P_0 = 10^6$.

Next, using $\hat{\theta}_{\hat{\mu}}$ given by (50), we rewrite (48) as

$$J_2(\hat{\theta}_{\hat{\mu}}, \hat{\mu}, \hat{b}) = \|\text{vec}^{-1}(\hat{\theta}_{\hat{\mu}}) - \hat{\mu}\hat{b}^T\|_F. \quad (51)$$

Then, Bernstein (2018, Fact 11.16.39, p. 906) implies that the rank-1 approximation of $\hat{\mu}\hat{b}^T$ that minimises J_2 is given by

$$\hat{\mu}\hat{b}^T = \sigma_{\max}(\text{vec}^{-1}(\hat{\theta}_{\hat{\mu}}))\psi_{1,1}(\text{vec}^{-1}(\hat{\theta}_{\hat{\mu}}))\psi_{r,1}(\text{vec}^{-1}(\hat{\theta}_{\hat{\mu}}))^T, \quad (52)$$

where $\psi_{1,1}(A)$ denotes the first left singular vector of A and $\psi_{r,1}(A)$ denotes the first right singular vector of A . Since $\hat{\mu}$ and \hat{b} are not separately identifiable from (52), choosing an arbitrary nonzero scaling parameter $\hat{\beta} \in \mathbb{R}$ and using it to separate (52) yields

$$\hat{\mu} = \hat{\beta}\sigma_{\max}(\text{vec}^{-1}(\hat{\theta}_{\hat{\mu}}))\psi_{1,1}(\text{vec}^{-1}(\hat{\theta}_{\hat{\mu}})), \quad (53)$$

$$\hat{b} = \frac{1}{\hat{\beta}}\psi_{r,1}(\text{vec}^{-1}(\hat{\theta}_{\hat{\mu}})). \quad (54)$$

Finally, if $\hat{\theta}_{\hat{v}}$ given by (50) is nonzero, then it follows from (45) that $\mathbf{1}_{1 \times \hat{n}}\hat{b}$ is nonzero, and thus \hat{v} is given by

$$\hat{v} = \frac{\hat{\theta}_{\hat{v}}}{\mathbf{1}_{1 \times \hat{n}}\hat{b}}. \quad (55)$$

Note that $\hat{\beta}$ is unidentifiable, and thus it can be chosen arbitrarily.

6. Mixed-integer optimisation for system identification

The minimisation of (39) in Section 5 depends on the chosen model parameters $\hat{n}, \hat{d}, \hat{c}$, and \hat{r} . In this section, a mixed-integer approach is used to determine optimal model parameters $\hat{n}, \hat{d}, \hat{c}$, and \hat{r} such that the output of the identified model \mathcal{M} parameterised by the estimates $\hat{a}, \hat{b}, \hat{v}$, and $\hat{\mu}$ matches the output of \mathcal{S} .

In order to constrain the width of the partitions in \hat{c} used to define CPA function ϕ , let $\hat{\varepsilon} > 0$ denote the minimum partition width. Furthermore, let $\hat{\lambda}$ be an integer such that $\hat{\lambda}\hat{\varepsilon}$ is the uniform distance between consecutive break points in \hat{c} , and let \hat{v}_n and \hat{v}_p denote the number of negative and positive components in \hat{c} , respectively. With this notation, (28) can be written as

$$\begin{aligned} \hat{c} &= \hat{\varepsilon}[-\hat{v}_n\hat{\lambda} \quad -(\hat{v}_n - 1)\hat{\lambda} \quad \cdots \quad (\hat{v}_p - 1)\hat{\lambda} \quad \hat{v}_p\hat{\lambda}]^T \\ &\in \mathbb{R}^{\hat{v}_n + \hat{v}_p + 1}, \end{aligned} \quad (56)$$

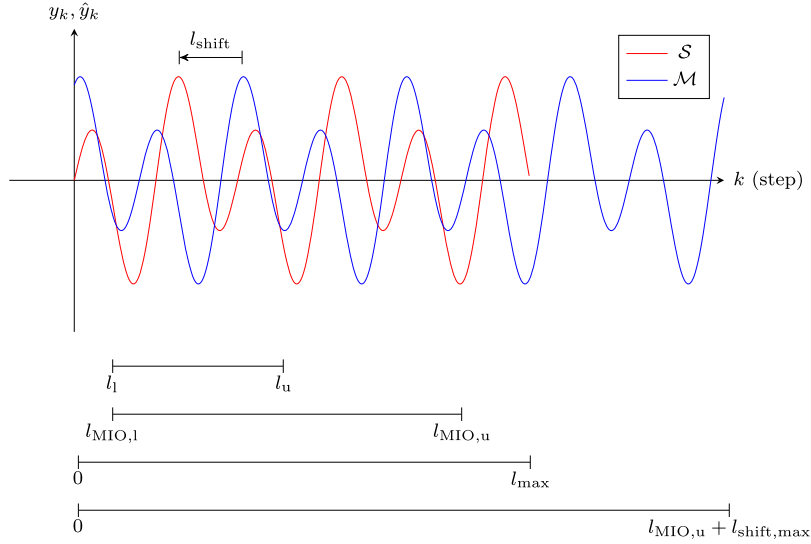


Figure 5. Output y_k of system \mathcal{S} for all $k \in [0, l_{\max}]$ available for MIO-ID and output \hat{y}_k of estimated DTLI/CPA model \mathcal{M} for all $k \in [0, l_{\text{MIO},u} + l_{\text{shift},\max}]$ obtained by propagating (26). J in (39) is computed using y_k for all $k \in [l_1, l_u]$, and J_{MIO} in (57) is computed using y_k for all $k \in [l_{\text{MIO},l}, l_{\text{MIO},u}]$. To compute J_{MIO} , the output \hat{y} of \mathcal{M} is shifted by up to $l_{\text{shift},\max} - 1$ steps to minimise the difference between \hat{y} and the output y of \mathcal{S} . Note that l_{shift} is the number of shift steps that minimise the difference between y and \hat{y} .

and thus $\hat{p} = \hat{v}_n + \hat{v}_p + 1$ and $\hat{r} = \hat{v}_n + 1$. Since \hat{e} is arbitrarily chosen, note that (56) requires estimates of only $\hat{\lambda}$, \hat{v}_n , and \hat{v}_p . In this paper, $\hat{e} = 10^{-3}$.

Next, suppose y_k for all $k \in [0, l_{\max}]$ are the measurements available to use for identification, such that $l_{\max} \geq l_u$. Given $\hat{n}, \hat{d}, \hat{\lambda}, \hat{v}_n, \hat{v}_p$, let $\hat{a}, \hat{b}, \hat{v}, \hat{\mu}$ minimise (39), let $l_{\text{MIO},u} > l_{\text{MIO},l} \geq \hat{n} + \hat{d} + 1$, such that $l_{\text{MIO},u} \leq l_{\max}$ and let $l_{\text{shift},\max}$ be the maximum time-step shift. Then, we define the cost function

$$J_{\text{MIO}} \triangleq \|Y_{\text{MIO}} - \hat{Y}_{\text{MIO},l_{\text{shift}}}\|_2, \quad (57)$$

where

$$Y_{\text{MIO}} \triangleq \begin{bmatrix} y_{l_{\text{MIO},l}} \\ \vdots \\ y_{l_{\text{MIO},u}} \end{bmatrix} \in \mathbb{R}^{l_{\text{MIO},u} - l_{\text{MIO},l} + 1}, \quad (58)$$

$$\hat{Y}_{\text{MIO},l_{\text{shift}}} \triangleq \begin{bmatrix} \hat{y}_{l_{\text{MIO},l} - l_{\text{shift}}} \\ \vdots \\ \hat{y}_{l_{\text{MIO},u} - l_{\text{shift}}} \end{bmatrix} \in \mathbb{R}^{l_{\text{MIO},u} - l_{\text{MIO},l} + 1}, \quad (59)$$

$$l_{\text{shift}} \triangleq \underset{l_{\text{shift}} \in [0, l_{\text{shift},\max}]}{\operatorname{argmin}} \|Y_{\text{MIO}} - \hat{Y}_{\text{MIO},l_{\text{shift}}}\|_2, \quad (60)$$

subject to

$$\hat{d} \geq 0, \quad (61)$$

$$\hat{n}, \hat{\lambda}, \hat{v}_n, \hat{v}_p > 0, \quad (62)$$

$$\hat{n}, \hat{d}, \hat{\lambda}, \hat{v}_n, \hat{v}_p \in \mathbb{N}_0. \quad (63)$$

Note that J_{MIO} considers shifts of \hat{y} relative to y by up to $l_{\text{shift},\max}$ steps using data y_k for all $k \in [l_{\text{MIO},l}, l_{\text{MIO},u}]$, and that (39) is computed using y_k for all $k \in [l_1, l_u]$. Figure 5 illustrates the data sets used to compute J_{MIO} .

To perform *mixed-integer-optimisation identification* (MIO-ID), we use an integer optimisation algorithm to minimise J_{MIO}

over $\hat{n}, \hat{d}, \hat{\lambda}, \hat{v}_n$, and \hat{v}_p . At each iteration, a DTLI/CPA model is estimated along with its associated J_{MIO} cost. Let $\ell \in \mathbb{N}_0$ be an MIO-ID iteration, and let $\hat{n}_\ell, \hat{d}_\ell, \hat{\lambda}_\ell, \hat{v}_{n,\ell}, \hat{v}_{p,\ell}, \hat{a}_\ell, \hat{b}_\ell, \hat{v}_\ell, \hat{\mu}_\ell$ and $J_{\text{MIO},\ell}$ be the DTLI/CPA parameters estimated at the ℓ th MIO-ID iteration and their associated cost obtained using (57). For all $\ell \geq 1$, $\hat{n}_\ell, \hat{d}_\ell, \hat{\lambda}_\ell, \hat{v}_{n,\ell}, \hat{v}_{p,\ell}$ are determined by a *1-step mixed-integer search* (ISMIS) algorithm with input $J_{\text{MIO},i}, \hat{n}_i, \hat{d}_i, \hat{\lambda}_i, \hat{v}_{n,i}, \hat{v}_{p,i}$ for all $i \in [0, \ell - 1]$. For $\ell = 0$, the ISMIS function initialises $\hat{n}_0, \hat{d}_0, \hat{\lambda}_0, \hat{v}_{n,0}, \hat{v}_{p,0}$ randomly. Then, for all $\ell \in \mathbb{N}_0$, Algorithm 1 shows how $J_{\text{MIO},\ell}, \hat{a}_\ell, \hat{b}_\ell, \hat{v}_\ell$, and $\hat{\mu}_\ell$ are computed using $\hat{n}_\ell, \hat{d}_\ell, \hat{\lambda}_\ell, \hat{v}_{n,\ell}, \hat{v}_{p,\ell}$ as input. Note that $\hat{a}_\ell, \hat{b}_\ell, \hat{v}_\ell$, and $\hat{\mu}_\ell$ are estimated by minimising (39) using the least-squares optimisation technique in Section 5.

The MIO-ID process terminates at step $\ell \geq 1$ when either $J_{\text{MIO},\ell-1} < J_{\min}$ or $\ell > \ell_{\max}$, where J_{\min} is a chosen minimal cost function value and ℓ_{\max} is the chosen maximum number of optimisation iterations. Then, the identified DTLI/CPA model \mathcal{M} is characterised by the estimated parameters $\hat{n} = \hat{n}_j, \hat{d} = \hat{d}_j, \hat{\lambda} = \hat{\lambda}_j, \hat{v}_n = \hat{v}_{n,j}, \hat{v}_p = \hat{v}_{p,j}, \hat{a} = \hat{a}_j, \hat{b} = \hat{b}_j, \hat{v} = \hat{v}_j$, and $\hat{\mu} = \hat{\mu}_j$, where

$$j = \underset{i \in [0, \ell-1]}{\operatorname{argmin}} J_{\text{MIO},i}. \quad (64)$$

The flow chart shown in Figure 6 summarises MIO-ID.

The ISMIS algorithm, which searches through the $\hat{n}, \hat{d}, \hat{\lambda}, \hat{v}_n, \hat{v}_p$ variable space, is a single step of a derivative-free mixed-integer optimisation algorithm. To reduce the optimisation time, the search space is constrained by setting minimum and maximum feasible values of $\hat{n}, \hat{d}, \hat{\lambda}, \hat{v}_n$, and \hat{v}_p , which implies that the values of l_1 and $l_{\text{MIO},l}$ need to be chosen to be greater than the sum of the maximum values set for \hat{n} and \hat{d} . In this paper, the ISMIS algorithm consists of a single step of a mixed-integer genetic algorithm and is implemented in Matlab by running a single optimisation iteration of the `surrogateopt`

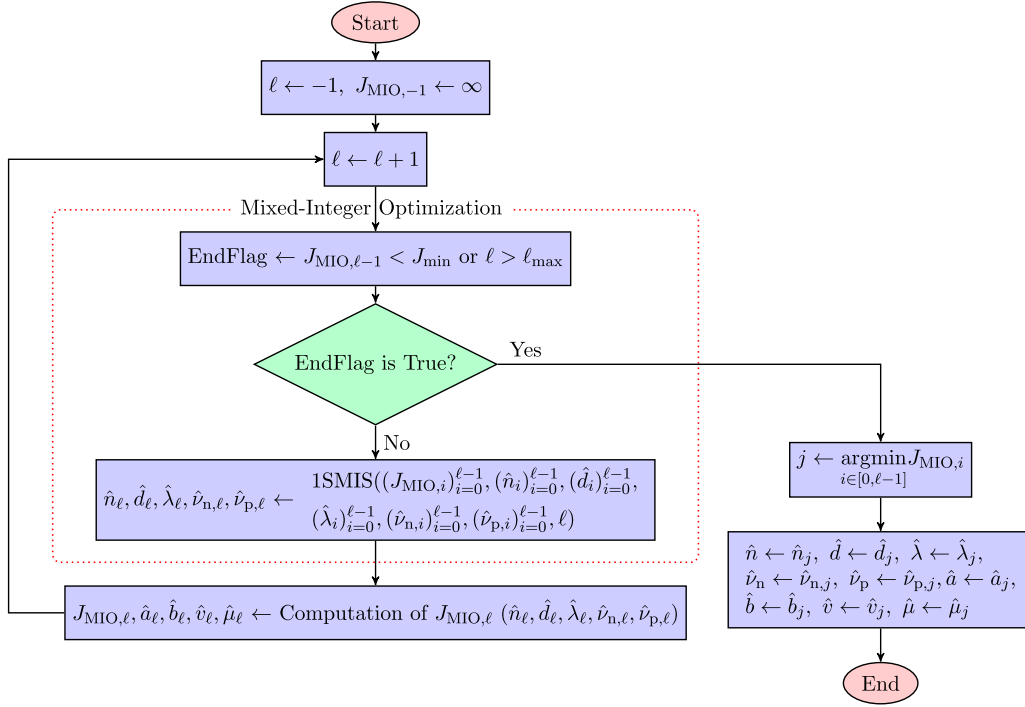


Figure 6. Flow chart of mixed-integer-optimisation identification (MIO-ID).

function. Note that `surrogateopt` chooses the initial values of \hat{n} , \hat{d} , $\hat{\lambda}$, \hat{v}_n , and \hat{v}_p based on their corresponding minimum and maximum feasible values. The choice of certain optimisation parameters can determine the resulting identified DTLI/CPA model. In that regard, the following suggestions may improve the identification results:

- Choosing l_l and l_u to include the transient response of system \mathcal{S} , as shown in Example 7.2.
- In most cases, choosing $l_l = l_{\text{MIO},l}$ and $l_u = l_{\text{MIO},u}$ will suffice. However, in cases where the oscillatory behaviour displayed by the output of system \mathcal{S} is irregular, l_l and l_u may be chosen to include a representative waveform, while $l_{\text{MIO},l}$ and $l_{\text{MIO},u}$ may be chosen to include more periods of the waveform, as shown in Example 11.2.
- Increasing the maximum values of \hat{n} and \hat{d} in the case where the output of system \mathcal{S} displays richer frequency content, as shown in the examples in Sections 10 and 11.
- Let z be given by (19) with y as the output of system \mathcal{S} and $d = 0$. Then, the maximum values of $\hat{\lambda}$, \hat{v}_n , and \hat{v}_p can be chosen so that the values of z are within $-\hat{e}\hat{v}_n\hat{\lambda}$ and $\hat{e}\hat{v}_p\hat{\lambda}$.

7. Application of MIO-ID to FTDDTL systems

In this section, we apply MIO-ID to FTDDTL systems. Since these systems have the form of the DTLI model, we evaluate the accuracy of MIO-ID by comparing the estimates \hat{G} and $\hat{\phi}$ with G and ϕ , respectively. Hence, in these examples, the unidentifiable parameter $\hat{\beta}$ is chosen to minimise the root-mean-square (RMS) fit between ϕ and $\hat{\phi}$. Furthermore, the power spectral density (PSD) and the waveforms of the outputs, the nonlinearities, and the frequency responses of the linear dynamics of FTDDTL system \mathcal{S} and the estimated DTLI/CPA model \mathcal{M} are

Table 1. Examples with FTDDTL systems.

Example	System type	n	d	SNR (dB)	ϕ
7.1	FTDDTL	2	4	∞ and 30	CPA, monotonic, odd
7.2		3	4		C^∞ monotonic, not odd
7.3		6	0		C^∞ nonmonotonic, odd

compared. Table 1 summarises details of the FTDDTL systems considered in this section, including the signal-to-noise ratio (SNR) considered in each example.

All computational results in this paper were obtained using a PC running Windows 10 Education, version 21H2, OS build 19044.1586 with 8-core 16-thread AMD Ryzen 3700X running at 3.59 GHz and 32GB DDR4 3600 MHz RAM running in dual channel with MATLAB version R2020a Update 7.

Example 7.1: FTDDTL with monotonic, odd ϕ

Consider the FTDDTL system \mathcal{S} with $d = 4$,

$$G(\mathbf{q}) = \frac{\mathbf{q} - 0.5}{\mathbf{q}^2 - 1.6\mathbf{q} + 0.8}, \quad (65)$$

and the CPA, monotonic, odd ϕ shown in Figure 7. The domain of ϕ is partitioned by $c = [-10 - 9 \dots 9 10]^T$, and ϕ is constructed such that, for all $i \in [1, 21]$, $\phi(c_i) = 18.75 \tanh(1.2c_i/2.5)$. To obtain data for identification, y_k is generated by simulating \mathcal{S} subject to $v = 37.5$. For MIO-ID, we let $\hat{n} \in [1, 10]$, $\hat{d} \in [0, 10]$, $\hat{\lambda} \in [1, 2000]$, $\hat{v}_n \in [1, 30]$, and $\hat{v}_p \in [1, 30]$, with $l_l = l_{\text{MIO},l} = 100$, $l_u = 500$, and $l_{\text{MIO},u} = 10,000$, that is, y_k for all $k \in [100, 500]$ is used for least-squares optimisation, and y_k and \hat{y}_k for all $k \in [100, 10,000]$ is used to compute J_{MIO} .

Figure 8 compares the response of the model \mathcal{M} identified using MIO-ID with the response of \mathcal{S} . The estimated DTLI/CPA

Algorithm 1: Computation of $J_{\text{MIO},\ell}$

Input: $\hat{n}_\ell, \hat{d}_\ell, \hat{\lambda}_\ell, \hat{v}_{n,\ell}, \hat{v}_{p,\ell}$
Output: $J_{\text{MIO},\ell}, \hat{a}_\ell, \hat{b}_\ell, \hat{v}_\ell, \hat{\mu}_\ell$

- 1 $\hat{c}_\ell \leftarrow \hat{e} [-\hat{v}_{n,\ell}\hat{\lambda}_\ell \dots (\hat{v}_{n,\ell} - 1)\hat{\lambda}_\ell \dots (\hat{v}_{p,\ell} - 1)\hat{\lambda}_\ell \hat{v}_{p,\ell}\hat{\lambda}_\ell]^T$
- 2 $\hat{a}_\ell, \hat{b}_\ell, \hat{v}_\ell, \hat{\mu}_\ell \leftarrow \text{argmin}_{a^*, b^*, v^*, \mu^*} J(a^*, b^*, v^*, \mu^*)$
 \triangleright Given $\hat{n}_\ell, \hat{d}_\ell, \hat{c}_\ell$, and y_k for all $k \in [l, l_u]$, minimise (39) using the least-squares optimisation technique in Section 5.
- 3 $\hat{y} \leftarrow [0 \dots 0]^T \in \mathbb{R}^{l_{\text{MIO},u} + l_{\text{shift},\max}}$
- 4 **for** $k \leftarrow \hat{n}_\ell + \hat{d}_\ell + 1$ **to** $l_{\text{MIO},u} + l_{\text{shift},\max}$ **do**
- 5 $\hat{y}_k \leftarrow \hat{\phi}_k^T [\hat{a}_\ell^T (\text{vec}(\hat{\mu}_\ell \hat{b}_\ell^T))^T \hat{v}_\ell \mathbf{1}_{1 \times \hat{n}_\ell} \hat{b}_\ell]^T$
 \triangleright Simulates DTL model with identified parameters given $\hat{n}_\ell, \hat{d}_\ell$, and \hat{c}_ℓ .
- 6 $\text{NaNFlag} \leftarrow \text{isNaN}(\hat{y})$
 \triangleright Determines whether the output of the simulated model yields a NaN response.
- 7 $J_{\text{MIO},\ell} \leftarrow \infty$
- 8 **if** NaNFlag is true **then**
- 9 **return** $J_{\text{MIO},\ell}, \hat{a}_\ell, \hat{b}_\ell, \hat{v}_\ell, \hat{\mu}_\ell$
- 10 **for** $j \leftarrow 0$ **to** l_{shift} **do**
- 11 $s_{\text{temp}} \leftarrow \sum_{k=l_{\text{MIO},l}}^{l_{\text{MIO},u}} (y_k - \hat{y}_{k+j})^2$
- 12 **if** $s_{\text{temp}} < J_{\text{MIO},\ell}$ **then**
- 13 $J_{\text{MIO},\ell} \leftarrow s_{\text{temp}}$
 \triangleright Local cost function computation with shift to account for the phase shift of the identified model.
- 14 **return** $J_{\text{MIO},\ell}, \hat{a}_\ell, \hat{b}_\ell, \hat{v}_\ell, \hat{\mu}_\ell$

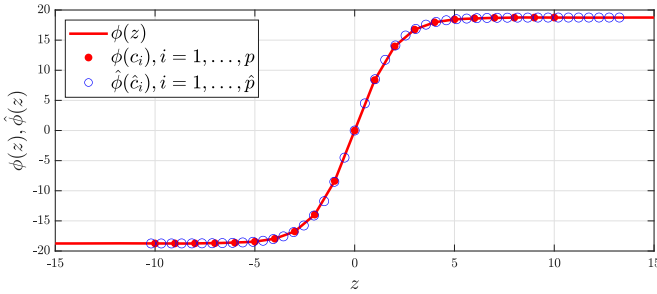


Figure 7. Example 7.1: Continuous piecewise-affine feedback mapping $\phi(z)$ partitioned by c and the estimated $\hat{\phi}(z)$ partitioned by \hat{c} .

model parameters are

$$\hat{G}(\mathbf{q}) = \frac{1.0002\mathbf{q} - 0.4996}{\mathbf{q}^2 - 1.6000\mathbf{q} + 0.8001}, \quad (66)$$

$\hat{d} = 4$, $\hat{v} = 37.46$, $\hat{v}_n = 20$, $\hat{v}_p = 26$, and $\hat{\phi}$ shown in Figure 8. The optimisation process required 30.29 s, during which J_{MIO} was computed 263 times. The minimum values of J_{MIO} up to each optimisation iteration ℓ are shown in Figure 9. Furthermore, the response of the identified model as the number of optimisation iterations increase is displayed in Figure 10 at three snapshots during MIO-ID, that is, for all $\ell \in \{1, 50, 250\}$.

Now, consider the output of \mathcal{S} with sensor noise with standard deviation $\sqrt{1.5}$, which yields an output signal with 30 dB SNR. Figure 11 compares the response of the model \mathcal{M} identified using MIO-ID in the presence of noisy measurements with the response of \mathcal{S} . The estimated DTLI/CPA model parameters are

$$\hat{G}(\mathbf{q}) = \frac{1.0911\mathbf{q}^2 - 0.1186\mathbf{q} - 0.2134}{\mathbf{q}^3 - 1.2092\mathbf{q}^2 + 0.1745\mathbf{q} + 0.3128}, \quad (67)$$

$\hat{d} = 4$, $\hat{v} = 34.345$, $\hat{v}_n = 4$, $\hat{v}_p = 12$, and $\hat{\phi}$ shown in Figure 11. The optimisation process required 95.55 s, during which J_{MIO} was computed 767 times.

Figure 12 shows the time domain responses of identified models estimated via MIO-ID by fixing \hat{n} and \hat{d} , such that $\{\hat{n}, \hat{d}\} \in \{1, 2, 3\} \times \{2, 3, 4\}$. Note that small changes in \hat{n} and \hat{d} can yield significantly different responses and thus different values of J_{MIO} . The complex changes of J_{MIO} over the $\hat{n}, \hat{d}, \hat{\lambda}, \hat{v}_n, \hat{v}_p$ parameter space motivated the use of a genetic algorithm for mixed-integer optimisation. Furthermore, note that, in the cases where $\hat{d} = d$ and $\hat{n} > n$, the responses of the identified models are very similar to those of \mathcal{S} , which implies that, under appropriate coefficients, higher order linear systems can approximate the response of lower order linear systems. \diamond

Example 7.2: FTDDTL system with monotonic, not odd ϕ

Consider the FTDDTL system \mathcal{S} with $d = 4$,

$$G(\mathbf{q}) = \frac{\mathbf{q}^2 - 2.3\mathbf{q} + 1.5725}{\mathbf{q}^3 - 2.35\mathbf{q}^2 + 2\mathbf{q} - 0.6}, \quad (68)$$

and a C^∞ , monotonic, not odd ϕ , such that, for all $z \in \mathbb{R}$,

$$\phi(z) = 15 \tanh(1.2(z - 3)/2.5) + 2.2342. \quad (69)$$

To obtain data for identification, y_k is generated by simulating \mathcal{S} subject to $v = 40$. For identification, we let $\hat{n} \in [1, 20]$, $\hat{d} \in [0, 20]$, $\hat{\lambda} \in [1, 2000]$, $\hat{v}_n \in [1, 30]$, and $\hat{v}_p \in [1, 30]$, with $l_l = l_{\text{MIO},l} = 100$, $l_u = 1500$, and $l_{\text{MIO},u} = 10,000$, that is, y_k for all $k \in [100, 1500]$ is used for least-squares optimisation, and y_k and \hat{y}_k for all $k \in [100, 10,000]$ is used to compute J_{MIO} . Figure 13 compares the response of the model \mathcal{M} identified

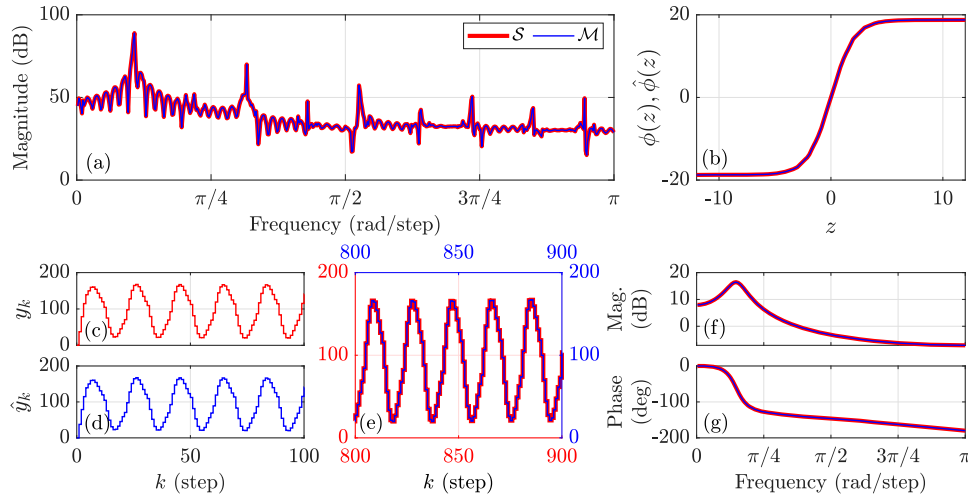


Figure 8. Example 7.1: MIO-ID of FTDDL system using noiseless measurements. (a) compares the PSD of the output of \mathcal{S} with the PSD of the output of \mathcal{M} . (b) Shows ϕ of \mathcal{S} and $\hat{\phi}$ of \mathcal{M} . (c) Shows the output y_k of \mathcal{S} with $v = 37.5$ for all $k \in [0, 100]$. (d) Shows the output \hat{y}_k of \mathcal{M} with $\hat{v} = 37.46$. (e) Shows the output y_k of \mathcal{S} and the output \hat{y}_k of \mathcal{M} for all $k \in [800, 900]$. (f,g) Compare the frequency responses G and \hat{G} .

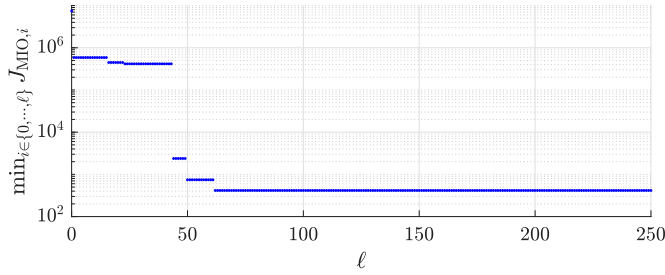


Figure 9. Example 7.1: Minimal cost $\min_{i \in [0, \ell]} J_{\text{MIO},i}$ up to iteration ℓ used in MIO-ID. The identified model \mathcal{M} , whose response is shown in Figure 8 is obtained by minimising (57).

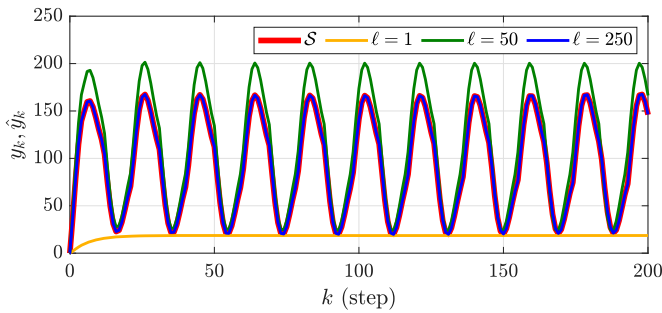


Figure 10. Example 7.1: Responses of \mathcal{S} and the identified model \mathcal{M} that minimises J_{MIO} as the number of optimisation iterations increases. The responses of \mathcal{M} are displayed for all $\ell \in \{1, 50, 250\}$.

using MIO-ID with the response of \mathcal{S} . The estimated DTLL/CPA model parameters are

$$\hat{G}(\mathbf{q}) = \frac{0.1209\mathbf{q}^2 + 0.1204\mathbf{q} + 0.1043}{1.0000\mathbf{q}^3 - 0.5577\mathbf{q}^2 + 0.0173\mathbf{q} - 0.0494},$$

$\hat{d} = 17$, $\hat{v} = 39.5712$, $\hat{v}_n = 5$, $\hat{v}_p = 6$, and $\hat{\phi}$ shown in Figure 13. Note that, although the MIO-ID parameter estimates are different from those of \mathcal{S} , the output of the identified system \mathcal{M} closely matches that of \mathcal{S} .

Next, consider the output of \mathcal{S} with sensor noise with standard deviation $\sqrt{40}$, which yields an output signal with 30 dB SNR. Figure 14 compares the response of the model \mathcal{M} identified using MIO-ID in the presence of noisy measurements with the response of \mathcal{S} . The estimated DTLL/CPA model parameters are $\hat{n} = 8$, $\hat{d} = 9$, $\hat{v} = 60.1698$, $\hat{v}_n = 8$, $\hat{v}_p = 12$, and $\hat{\phi}$ shown in Figure 14. Similarly to the noiseless case, while the parameters of the identified model differ from those of \mathcal{S} , the output of the identified system \mathcal{M} closely matches that of \mathcal{S} .

Now, we show that the parameters of the identified system estimated by MIO-ID can match those of \mathcal{S} in the case where the input is known and nonconstant. In order to do this, the inner-loop nonlinear least-squares optimisation shown in Section 5 is modified for nonconstant v , as shown in Section 5 of Paredes and Bernstein (2020). Consider the system (68) simulated with v as a Gaussian random variable with mean 5 and standard deviation $\sqrt{1.5}$. Figure 15 compares the response of the model \mathcal{M} identified using MIO-ID with the response of \mathcal{S} , both driven by the constant input $v = \hat{v} = 40$. The estimated DTLL/CPA model parameters are

$$\hat{G}(\mathbf{q}) = \frac{1.0147\mathbf{q}^2 - 2.3314\mathbf{q} + 1.5921}{1.0000\mathbf{q}^3 - 2.3500\mathbf{q}^2 + 1.9999\mathbf{q} - 0.6000}, \quad (70)$$

$\hat{d} = 4$, $\hat{v}_n = 6$, $\hat{v}_p = 10$, and $\hat{\phi}$ shown in Figure 15. Note that, unlike the cases where the input is assumed to be unknown and constant, the estimated DTLL/CPA model parameters are similar to those of \mathcal{S} , which shows that MIO-ID is more accurate when the input is known and more persistent, as shown in Figure 16.

Next, we consider the identification of \mathcal{S} using noiseless measurements that include the transient response of the system. Let $l_1 = \hat{n} + \hat{d} + 1$, $l_u = 1500$, $l_{\text{MIO},l} = 100$, and $l_{\text{MIO},u} = 10,000$, that is, y_k for all $k \in [\hat{n} + \hat{d} + 1, 1500]$ is used for least-squares optimisation, and y_k and \hat{y}_k for all $k \in [100, 10,000]$ is used to compute J_{MIO} , such that the transient response of \mathcal{S} is used for identification, unlike previous cases. Figure 17 compares the response of the model \mathcal{M} identified using MIO-ID in the presence of noiseless measurements that include the transient

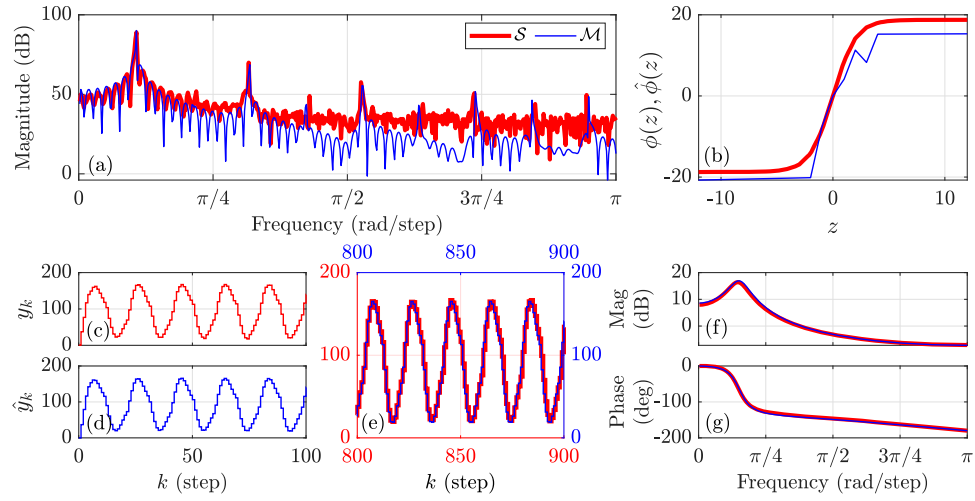


Figure 11. Example 7.1: MIO-ID of FTDDL system using noisy measurements. (a) compares the PSD of the output of S with the PSD of the output of M . (b) Shows ϕ of S and $\hat{\phi}$ of M . (c) Shows the output y_k of S with $v = 37.5$ for all $k \in [0, 100]$. (d) Shows the output \hat{y}_k of M with $\hat{v} = 34.345$ for all $k \in [0, 100]$. (e) Shows the output y_k of S and the output \hat{y}_k of M for all $k \in [800, 900]$. (f,g) Compare the frequency responses of G and \hat{G} .

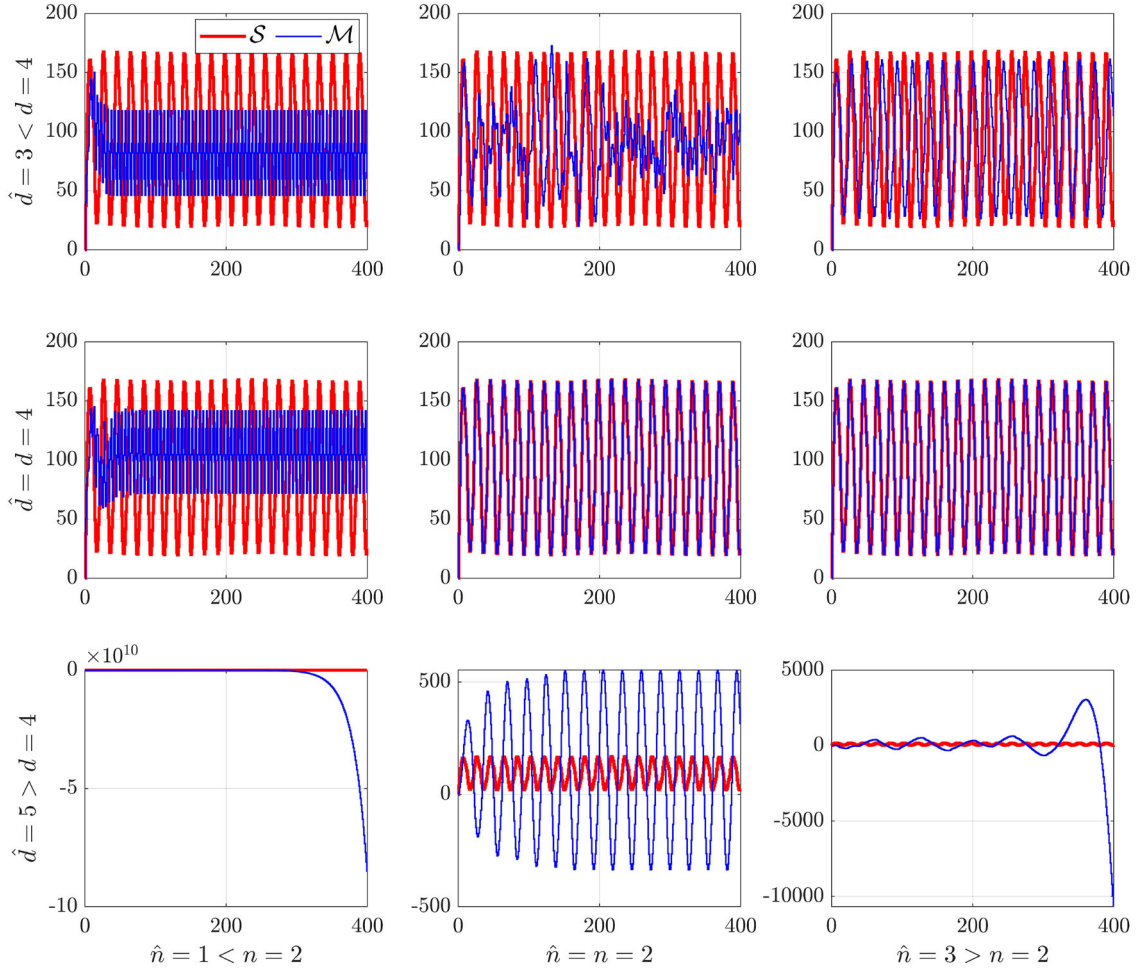


Figure 12. Example 7.1: MIO-ID of FTDDL system with fixed \hat{n} and \hat{d} , such that $\{\hat{n}, \hat{d}\} \in \{1, 2, 3\} \times \{2, 3, 4\}$. These plots compare the output \hat{y}_k of the identified model M with the output y_k of system S for all $k \in [0, 400]$.

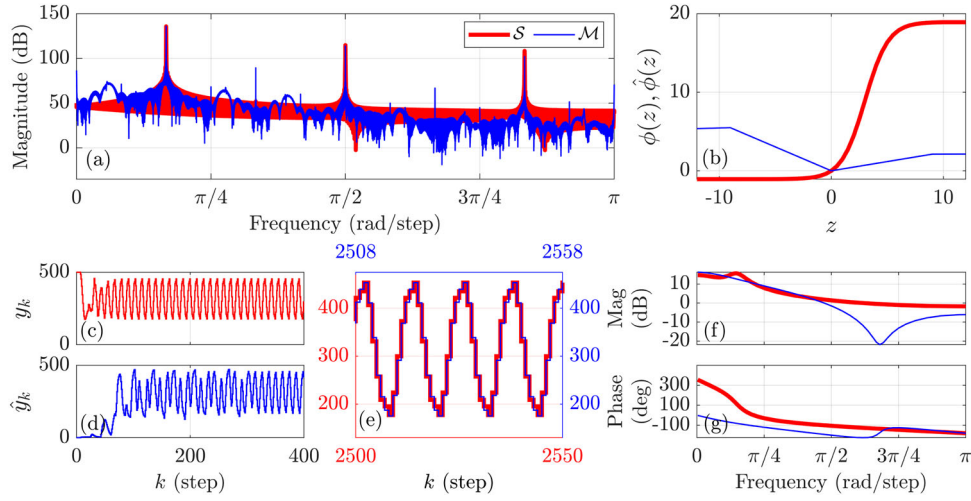


Figure 13. Example 7.2: MIO-ID of FTDDTL system using noiseless measurements. (a) compares the PSD of the output of S with the PSD of the output of M . (b) Shows ϕ of S and $\hat{\phi}$ of M . (c) Shows the output y_k of S with $v = 40$ for all $k \in [0, 1000]$. (d) Shows the output \hat{y}_k of M with $\hat{v} = 39.5712$ for all $k \in [0, 1000]$. (e) Shows the output y_k of S for all $k \in [2500, 2550]$ and the output \hat{y}_k of M for all $k \in [2508, 2558]$. (f,g) Compare the frequency responses of G and \hat{G} .

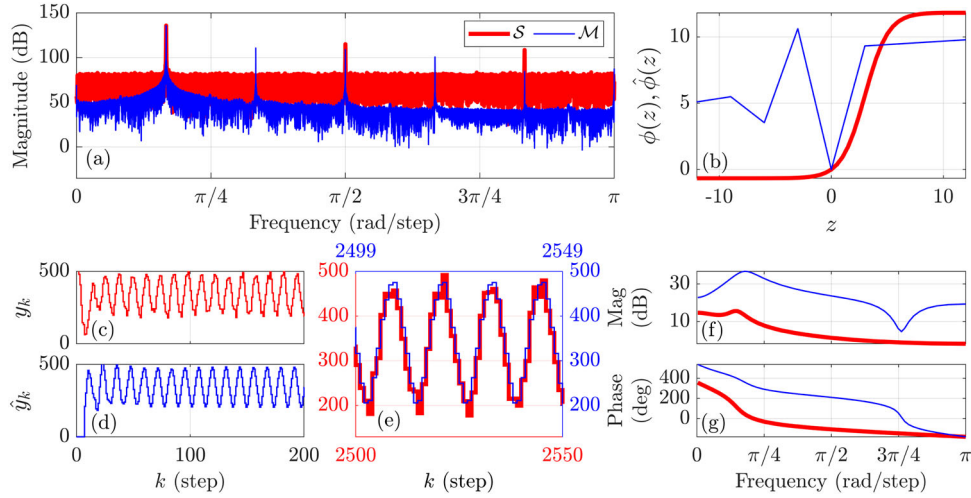


Figure 14. Example 7.2: MIO-ID of FTDDTL using noisy measurements. (a) compares the PSD of the output of S with the PSD of the output of M . (b) Shows ϕ of S and $\hat{\phi}$ of M . (c) Shows the output y_k of S with $v = 40$ for all $k \in [0, 200]$. (d) Shows the output \hat{y}_k of M with $\hat{v} = 60.1698$ for all $k \in [0, 200]$. (e) Shows the output y_k of S for all $k \in [2500, 2550]$ and the output \hat{y}_k of M , for all $k \in [2499, 2549]$. (f,g) Compare the frequency responses of G and \hat{G} .

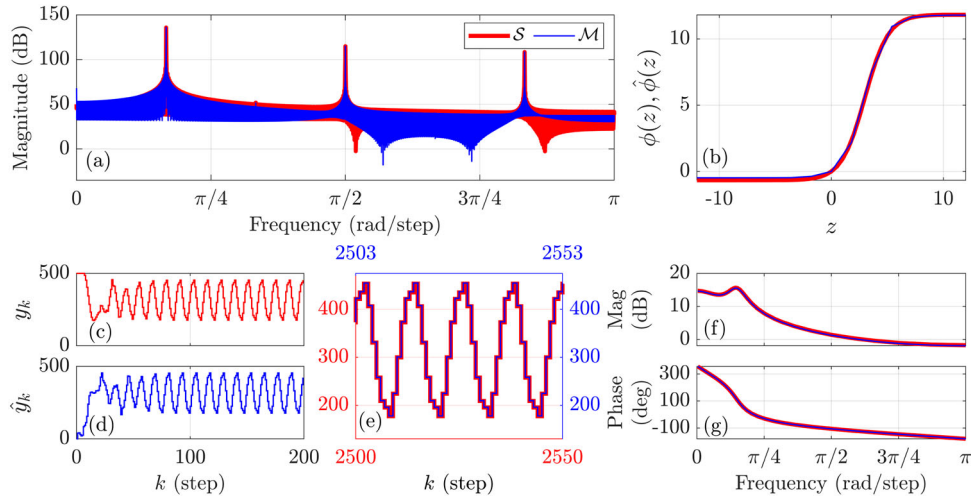


Figure 15. Example 7.2: MIO-ID of FTDDTL system using noiseless measurements with a Gaussian random variable as input. (a) Compares the PSD of the output of S with the PSD of the output of M . (b) Shows ϕ of S and $\hat{\phi}$ of M . (c) Shows the output y_k of S with $v = 40$ for all $k \in [0, 200]$. (d) Shows the output \hat{y}_k of M with $\hat{v} = 40$ for all $k \in [0, 200]$. (e) Shows the output y_k of S for all $k \in [2500, 2550]$ and the output \hat{y}_k for M for all $k \in [2503, 2553]$. (f,g) Compare the frequency responses of G and \hat{G} .

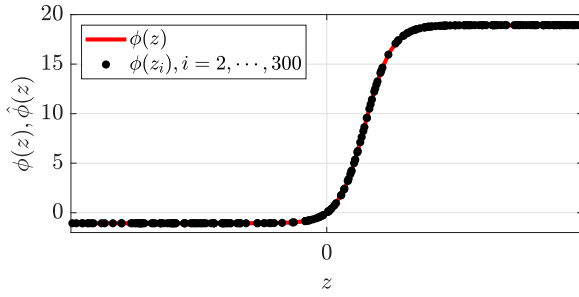


Figure 16. Example 7.2: (z_k, u_k) pairs from S for all $k \in [2, 300]$, plotted with ϕ using Gaussian white noise as input. Note the persistency in the data.

response with the response of S . The estimated DTLI/CPA model parameters are

$$\hat{G}(q) = \frac{1.0147q^2 - 2.2974q + 1.5604}{1.0000q^3 - 2.3499q^2 + 1.9997q - 0.5999}, \quad (71)$$

$\hat{d} = 4$, $\hat{v} = 39.87$, $\hat{v}_n = 20$, $\hat{v}_p = 22$, and $\hat{\phi}$ shown in Figure 17. Furthermore, Figure 18 plots the (z_k, u_k) pairs from S for all $k \in [2, 300]$, which implies that the $\hat{\phi}$ estimate of ϕ is more accurate in regions with more data points. Compared to the identification results in Figure 13, the estimated DTLI/CPA model parameters are similar to those of S when the transient response is included in identification data window, which show that MIO-ID is more accurate when the measurements are more persistent.

Example 7.3: FTDDTL system with nonmonotonic, odd ϕ

Consider the FTDDTL system S with $d = 0$,

$$G(q) = \frac{q^2 + 1.5q + 0.8125}{q^6 - 3.5442q^5 + 5.21974q^4 - 3.92160q^3 + 1.5316q^2 - 0.2722q - 0.02153}, \quad (72)$$

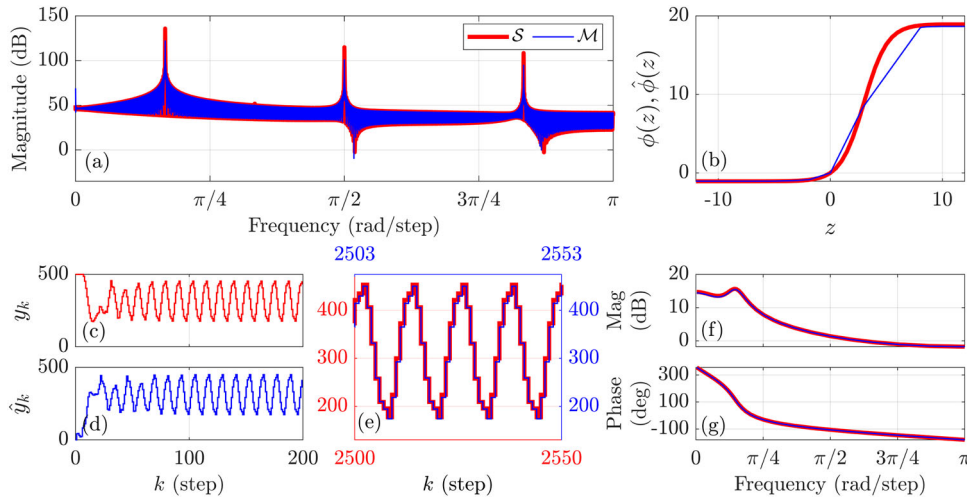


Figure 17. Example 7.2: MIO-ID of FTDDTL system using noiseless measurements that include the transient response of the system. (a) Compares the PSD of the output of S with the PSD of the output of \mathcal{M} . (b) Shows ϕ of S and $\hat{\phi}$ of \mathcal{M} . (c) Shows the output y_k of S with $v = 40$ for all $k \in [0, 200]$. (d) Shows the output \hat{y}_k of \mathcal{M} with $\hat{v} = 39.87$ for all $k \in [0, 200]$. (e) Shows the output y_k of S for all $k \in [2500, 2550]$ and the output \hat{y}_k for \mathcal{M} for all $k \in [2503, 2553]$. (f,g) Compare the frequency responses of G and \hat{G} .

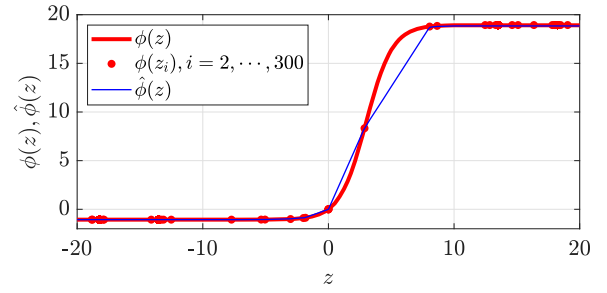


Figure 18. Example 7.2: (z_k, u_k) pairs from S for all $k \in [2, 300]$, plotted with ϕ and $\hat{\phi}$ obtained from MIO-ID of FTDDTL system using noiseless measurements that include the transient response of the system. Note that the $\hat{\phi}$ estimate of ϕ is less accurate in regions with scarce data points and large changes in ϕ , such as for all $z \in [0, 8]$. Note that $|z| \geq 20$ is truncated since they exceed the maximum possible estimates of $\hat{v}_n \hat{\lambda} / \hat{v}_p \hat{\lambda}$ and are therefore saturated.

and the C^∞ , nonmonotonic, odd ϕ , such that, for all $z \in \mathbb{R}$,

$$\phi(z) = -\phi_{\max} \frac{1}{\sigma_\phi \sqrt{2\pi}} e^{-\frac{1}{2}((z+\mu_\phi)/\sigma_\phi)^2} + \phi_{\max} \frac{1}{\sigma_\phi \sqrt{2\pi}} e^{-\frac{1}{2}((z-\mu_\phi)/\sigma_\phi)^2}, \quad (73)$$

with $\phi_{\max} = 4$, $\sigma_\phi = 1.75$, and $\mu_\phi = 4$. To obtain data for identification, y_k is generated by simulating S subject to $v = 2$. For identification, we let $\hat{n} \in [1, 20]$, $\hat{d} \in [0, 20]$, $\hat{\lambda} \in [1, 2000]$, $\hat{v}_n \in [1, 30]$, and $\hat{v}_p \in [1, 30]$, with $l_l = l_{\text{MIO},l} = 100$, $l_u = 1500$, and $l_{\text{MIO},u} = 10,000$, that is, y_k for all $k \in [100, 1500]$ is used for least-squares optimisation, and y_k and \hat{y}_k for all $k \in [100, 10,000]$ is used to compute J_{MIO} . Figure 19 compares the response of the model \mathcal{M} identified using MIO-ID with the response of S . The estimated DTLI/CPA model parameters are

$$\hat{G}(q) = \frac{0.1228q + 0.1579}{q^2 - 1.5938q + 0.7528},$$

$\hat{d} = 4$, $\hat{v} = 19.6144$, $\hat{v}_n = 15$, $\hat{v}_p = 9$, and $\hat{\phi}$ shown in Figure 19. As in Example 7.2, although the MIO-ID parameter estimates

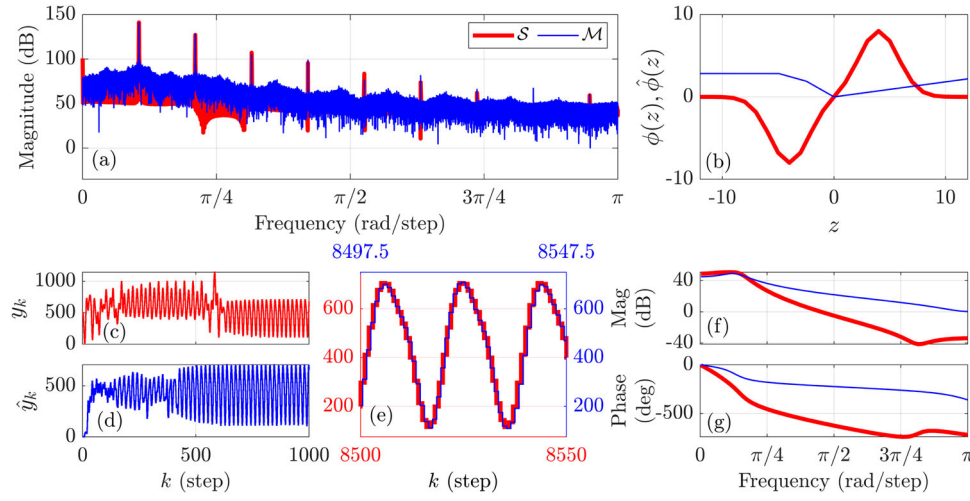


Figure 19. Example 7.3: MIO-ID of FTDDL system using noiseless measurements. (a) Compares the PSD of the output of S with the PSD of the output of M . (b) Shows ϕ of S and $\hat{\phi}$ of M . (c) Shows the output y_k of S with $v = 2$ for all $k \in [0, 1000]$. (d) Shows the output \hat{y}_k of M with $\hat{v} = 19.6144$ for all $k \in [0, 1000]$. (e) Shows the output y_k of S for all $k \in [8500, 8550]$ and the output \hat{y}_k of M for all $k \in [8496, 8546]$. (f,g) Compare the frequency responses of G and \hat{G} .

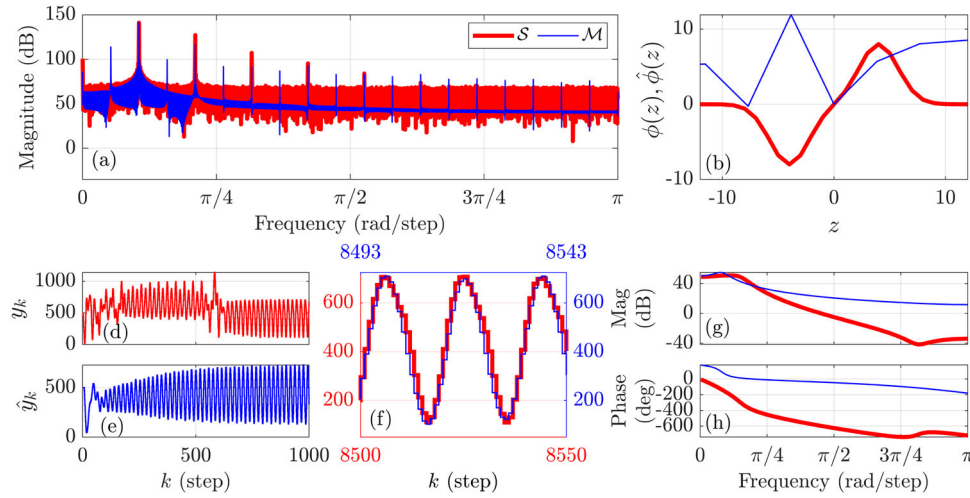


Figure 20. Example 7.3: MIO-ID of FTDDL system using noisy measurements. (a) Compares the PSD of the output of S with the PSD of the output of M . (b) Shows ϕ of S and $\hat{\phi}$ of M . (c) Shows the output y_k of S with $v = 2$ for all $k \in [0, 1000]$. (d) Shows the output \hat{y}_k of M with $\hat{v} = 9.03$ for all $k \in [0, 1000]$. (e) Shows the output y_k of S for all $k \in [8500, 8550]$ and the output \hat{y}_k of M for all $k \in [8493, 8543]$. (f,g) Compare the frequency responses of G and \hat{G} .

are different from those of S , the output of the identified system M closely matches that of S .

Next, consider the output of S with sensor noise with standard deviation $\sqrt{45}$, which yields an output signal with 30 dB SNR. Figure 20 compares the response of the model M identified using MIO-ID in the presence of noisy measurements with the response of S . The estimated DTLI/CPA model parameters are $\hat{n} = 9$, $\hat{d} = 10$, $\hat{v} = 9.03$, $\hat{v}_n = 9$, $\hat{v}_p = 20$, and $\hat{\phi}$ shown in Figure 20. Similarly to the noiseless case, while the parameters of the identified model differ from those of S , the output of the identified system M closely matches that of S .

Next, we show that the parameters of parameters of the identified system estimated by MIO-ID can match those of S in the case where the input is known and nonconstant, as in Example 7.2. Consider the system (72) simulated with v as a Gaussian random variable with mean 3 and standard deviation $\sqrt{5}$. Figure 21 compares the response of the model M identified using MIO-ID in the presence of noisy measurements with the response of S , both driven by the constant input $v = 5$. The

estimated DTLI/CPA model parameters are

$$\hat{G}(q) = \frac{4.3 \cdot 10^{-4} q^5 + 1.4 \cdot 10^{-5} q^4 - 8.2 \cdot 10^{-4} q^3 + 0.9872 q^2 + 1.4816 q + 0.8030}{q^6 - 3.5442 q^5 + 5.1973 q^4 - 3.9160 q^3 + 1.5317 q^2 - 0.2723 q + 0.0154},$$

$\hat{d} = 0$, $\hat{v}_n = 12$, $\hat{v}_p = 14$, and $\hat{\phi}$ shown in Figure 21. As in Example 7.2, MIO-ID is more accurate when the input is more persistent.

8. Application of MIO-ID to the logistic map

In this section, we apply MIO-ID to data obtained from the logistic map given by (7)–(9) under various parameters. Note that, although the logistic map is a DTL system, it does not include a washout filter, and thus it does not have the form of an FTDDL model. We thus set $\hat{\beta} = 1$. Table 2 summarises the details of the examples considered in this section.

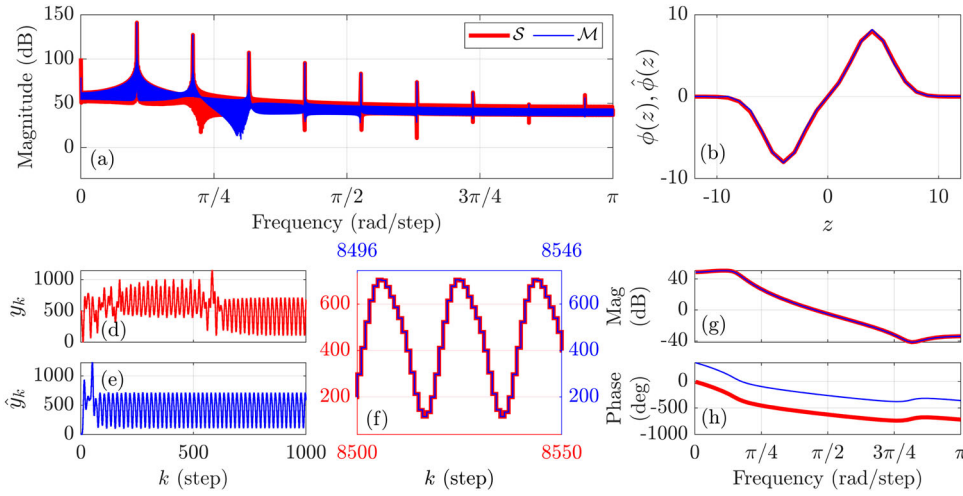


Figure 21. Example 7.3: MIO-ID of FTDDL system using noiseless measurements with Gaussian random variable as input. (a) Compares the PSD of the output of \mathcal{S} with the PSD of the output of \mathcal{M} . (b) Shows ϕ of \mathcal{S} and $\hat{\phi}$ of \mathcal{M} . (c) Shows the output y_k of \mathcal{S} with $v = 2$ for all $k \in [0, 1000]$. (d) Shows the output \hat{y}_k of \mathcal{M} with $\hat{v} = 2$ for all $k \in [0, 1000]$. (e) Shows the output y_k of \mathcal{S} for all $k \in [8500, 8550]$ and the output \hat{y}_k of \mathcal{M} for all $k \in [8498, 8548]$. (f,g) Compare the frequency responses of G and \hat{G} .

Table 2. Examples with logistic map.

Example	System type	Parameter	SNR (dB)	Remark
8.1.1	Logistic Map	$\gamma = 3$	∞	Response has a 2-step oscillation
8.1.2		$\gamma = 3.5$		Response has a 4-step oscillation
8.1.3		$\gamma = 3.565$		Response has a 8-step oscillation
8.1.4		$\gamma = 4$		Response is chaotic

Example 8.1: Logistic map

Let \mathcal{S} be the discrete-time model described by the logistic map is given by (7)–(9) where $\gamma \in \mathbb{R}$. Note that, in the case where $\gamma \in [3, 1 + \sqrt{6}]$, response of the logistic map approaches to a solution that oscillates between two γ -dependent values, that is, there exists $k_0 > 0$ such that, for all $k \geq k_0$,

$$y_k \in \left\{ \frac{1}{2} + \frac{1 - \sqrt{(\gamma - 3)(\gamma + 1)}}{2\gamma}, \frac{1}{2} + \frac{1 + \sqrt{(\gamma - 3)(\gamma + 1)}}{2\gamma} \right\}. \quad (74)$$

For all $k > 1$, the logistic map equation is propagated to obtain data. Since the value of γ determines the response of the logistic map, MIO-ID is applied to data obtained from the logistics map with $\gamma \in \{3, 3.5, 3.565, 4\}$.

Example 8.1.1: Logistic map with $\gamma = 3$

Let $\gamma = 3$ and $x_0 = 0.5$. For identification, we let $\hat{n} \in [1, 20]$, $\hat{d} \in [0, 20]$, $\hat{\lambda} \in [1, 50,000]$, $\hat{v}_n \in [1, 20]$, and $\hat{v}_p \in [1, 20]$, with $l_1 = l_{\text{MIO},l} = 3000$, $l_u = 3100$, and $l_{\text{MIO},u} = 10,000$ that is, y_k for all $k \in [3000, 3100]$ is used for least-squares optimisation, and y_k and \hat{y}_k for all $k \in [3000, 10,000]$ is used to compute J_{MIO} . Figure 22 compares the response of the model \mathcal{M} identified using MIO-ID with the response of \mathcal{S} . The estimated DTLI/CPA model parameters are $\hat{n} = 1$, $\hat{d} = 0$, $\hat{v}_n = 12$, $\hat{v}_p = 10$, $\hat{v} = -3.076$, \hat{G} with a frequency response shown in Figure 23, and $\hat{\phi}$ shown in Figure 23.

Example 8.1.2: Logistic map with $\gamma = 3.5$

Let $\gamma = 3.5$ and $x_0 = 0.5$. Note that, in the case where $\gamma \in (1 + \sqrt{6}, 3.544)$, the response of the logistic map has a 4-step oscillation. For identification, we let $\hat{n} \in [1, 50]$, $\hat{d} \in [0, 50]$, $\hat{\lambda} \in [1, 50,000]$, $\hat{v}_n \in [1, 20]$, and $\hat{v}_p \in [1, 20]$, with $l_1 = l_{\text{MIO},l} = 3000$, $l_u = 3100$, and $l_{\text{MIO},u} = 10,000$ that is, y_k for all $k \in [3000, 3100]$ is used for least-squares optimisation, and y_k and \hat{y}_k for all $k \in [3000, 10,000]$ is used to compute J_{MIO} . Figure 24 compares the response of the model \mathcal{M} identified using MIO-ID with the response of \mathcal{S} . The estimated DTLI/CPA model parameters are $\hat{n} = 1$, $\hat{d} = 1$, $\hat{v}_n = 3$, $\hat{v}_p = 2$, $\hat{v} = -2.8305$, \hat{G} with a frequency response shown in Figure 25, and $\hat{\phi}$ shown in Figure 25.

Example 8.1.3: Logistic map with $\gamma = 3.565$

Let $\gamma = 3.565$ and $x_0 = 0.5$. For this value of γ , the response of the logistic map has a 8-step oscillation. For identification, we let $\hat{n} \in [1, 50]$, $\hat{d} \in [0, 50]$, $\hat{\lambda} \in [1, 50,000]$, $\hat{v}_n \in [1, 20]$, and $\hat{v}_p \in [1, 20]$, with $l_1 = l_{\text{MIO},l} = 3000$, $l_u = 3100$, and $l_{\text{MIO},u} = 10,000$ that is, y_k for all $k \in [3000, 3100]$ is used for least-squares optimisation, and y_k and \hat{y}_k for all $k \in [3000, 10,000]$ is used to compute J_{MIO} . Figure 26 compares the response of the model \mathcal{M} identified using MIO-ID with the response of \mathcal{S} . The estimated DTLI/CPA model parameters are $\hat{n} = 2$, $\hat{d} = 0$, $\hat{v}_n = 14$, $\hat{v}_p = 19$, $\hat{v} = 5.0736$, \hat{G} with a frequency response shown in Figure 27, and $\hat{\phi}$ shown in Figure 27.

Example 8.1.4: Logistic map with $\gamma = 4$ (chaotic response)

Let $\gamma = 4$ and $x_0 = 0.1$. For this value of γ , the response of the logistic map is chaotic. For this example, we remove the washout filter in the DTLI/CPA model such that $y_f = y_d$, and the method in Section 5 is applied with $\hat{n} = 1$, $\hat{d} = 0$, $\hat{c} = [-1.2 \quad -1.19 \quad \dots \quad 1.19 \quad 1.2]$, $\hat{r} = 121$, $l_1 = 2$ and $l_u = 1500$. Figure 28 shows the response of the model \mathcal{M} , estimated using the method in Section 5, as well as the estimated nonlinearity. Note that (7)–(9) can be written as

$$x_{k+1} = \phi(x_k), \quad (75)$$

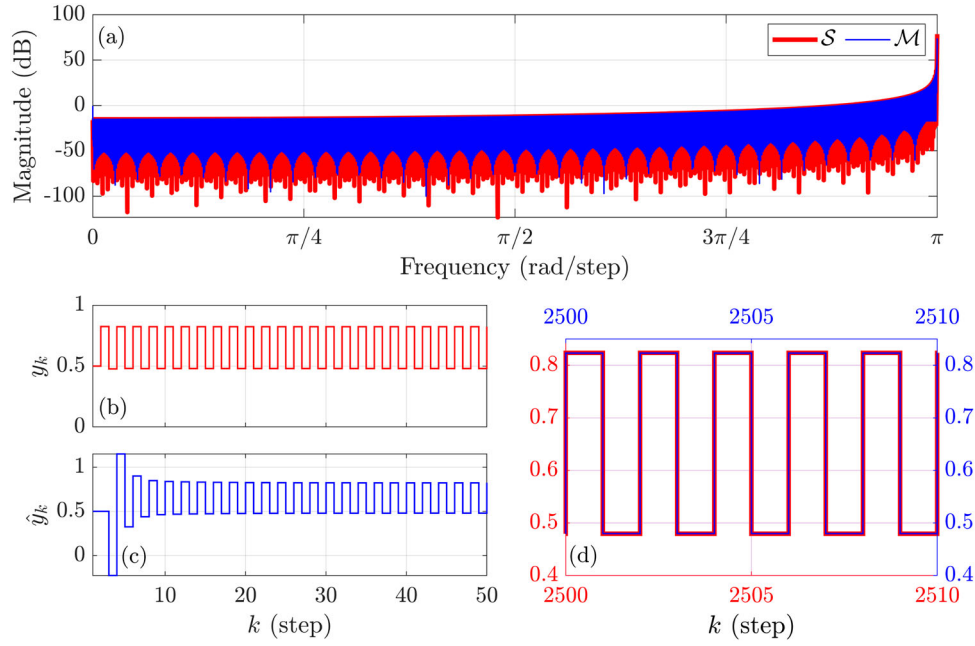


Figure 22. Example 8.1.1: MIO-ID of the logistic map equations (7)–(9) with $\gamma = 3$, using noiseless measurements. (a) Compares the PSD of the output of \mathcal{S} with the PSD of the output of \mathcal{M} . (b) Shows the output y_k of \mathcal{S} for all $k \in [0, 50]$. (c) Shows the output \hat{y}_k of \mathcal{M} with $\hat{\nu} = -3.076$ for all $k \in [0, 50]$. (d) Shows the output y_k of \mathcal{S} for all $k \in [2500, 2510]$, and the output \hat{y}_k of \mathcal{M} for all $k \in [2500, 2510]$.

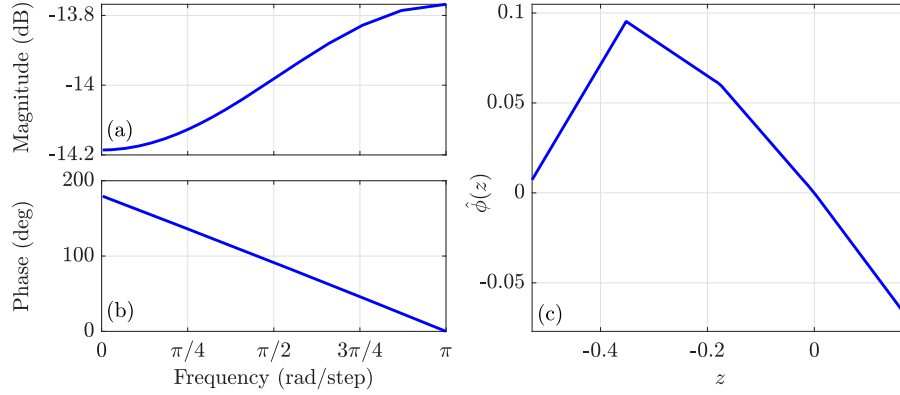


Figure 23. Example 8.1.1: MIO-ID of the logistic map equations (7)–(9) with $\gamma = 3$, using noiseless measurements. (a,b) Shows the frequency response of \hat{G} . (c) Shows the estimated nonlinearity $\hat{\phi}$.

where $\phi(x_k) = \gamma(x_k - x_k^2)$, which corresponds to the identified feedback nonlinearity, as shown in Figure 28. Since $x_k = y_k \in [0, 1]$ for all $k \geq 0$, the nonlinearity is identified within only this interval, remaining 0 otherwise.

9. Continuous-time Lur'e system

For all $t \geq 0$, consider the *continuous-time Lur'e* (CTL) system shown in Figure 29, which has the dynamics

$$\dot{x}(t) = Ax(t) + Bu(t) + Dv(t), \quad (76)$$

$$y(t) = Cx(t). \quad (77)$$

$$z(t) = Ex(t), \quad (78)$$

$$u(t) = \phi(z(t)), \quad (79)$$

where $x(t) \in \mathbb{R}^n$, $u(t) \in \mathbb{R}^m$, $v(t) \in \mathbb{R}$, $y(t) \in \mathbb{R}$, $z(t) \in \mathbb{R}^p$, $A \in \mathbb{R}^{n \times n}$, $B \in \mathbb{R}^{n \times m}$, $C \in \mathbb{R}^{1 \times n}$, $D \in \mathbb{R}^{n \times 1}$, $E \in \mathbb{R}^{p \times n}$, and $\phi :$

$\mathbb{R}^p \rightarrow \mathbb{R}^m$. Combining (76)–(79) yields

$$\dot{x}(t) = Ax(t) + B\phi(Ex(t)) + Dv(t), \quad (80)$$

$$y(t) = Cx(t). \quad (81)$$

It is assumed that, for all $T > 0$, (80), (81) has a unique solution on $[0, T]$. This assumption rules out equations that lack either uniqueness or global existence or both, such as $\dot{x} = \sqrt{|x|}$, $\dot{x} = x^2$, and $\dot{x} = x^{1/3} + x^3$.

Example 9.1: The dynamics of the van der Pol oscillator can be written as

$$\dot{x}(t) = \begin{bmatrix} 0 & 1 \\ -1 & 0 \end{bmatrix} x(t) + \begin{bmatrix} 0 \\ \gamma \end{bmatrix} \phi(x(t)), \quad (82)$$

$$y(t) = [1 \ 0]x(t), \quad (83)$$

$$\phi(x(t)) = (1 - x_1^2(t))x_2(t), \quad (84)$$

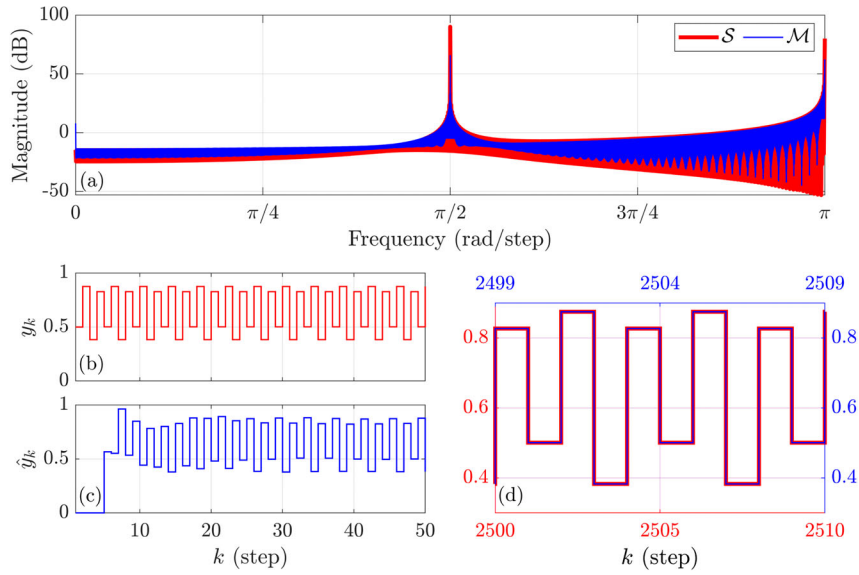


Figure 24. Example 8.1.2: MIO-ID of the logistic map equations (7)–(9) with $\gamma = 3.5$, using noiseless measurements. (a) Compares the PSD of the output of S with the PSD of the output of M . (b) Shows the output y_k of S for all $k \in [0, 50]$. (c) Shows the output \hat{y}_k of M with $\hat{v} = -2.8305$ for all $k \in [0, 50]$. (d) Shows the output y_k of S for all $k \in [2500, 2510]$, and the output \hat{y}_k of M for all $k \in [2502, 2512]$.

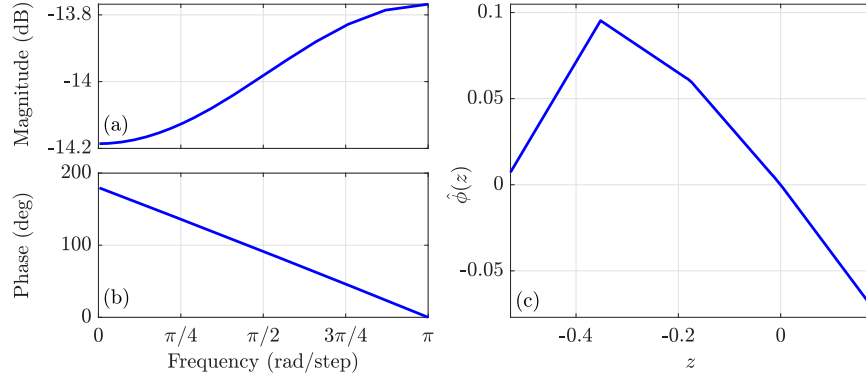


Figure 25. Example 8.1.2: MIO-ID of the logistic map equations (7)–(9) with $\gamma = 3.5$, using noiseless measurements. (a,b) Shows the frequency response of \hat{G} . (c) Shows the estimated nonlinearity $\hat{\phi}$.

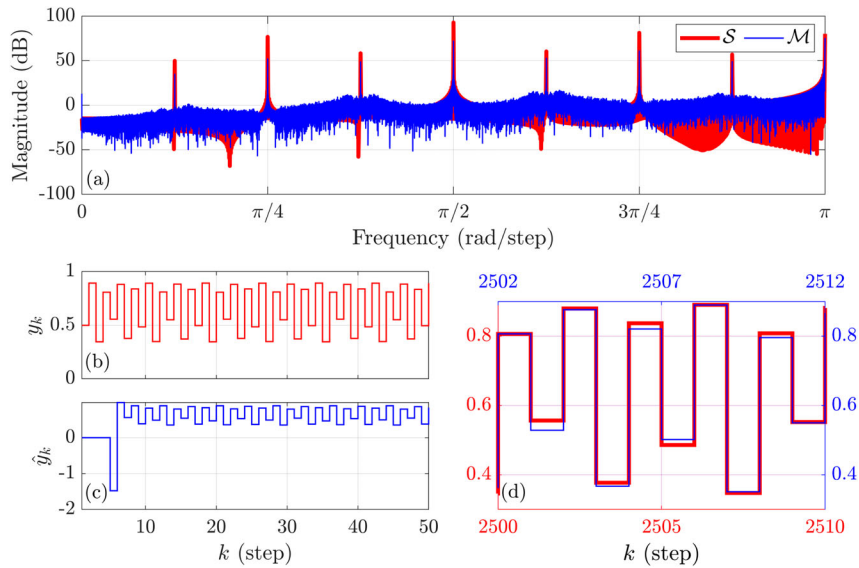


Figure 26. Example 8.1.3: MIO-ID of the logistic map equations (7)–(9) with $\gamma = 3.5$, using noiseless measurements. (a) Compares the PSD of the output of S with the PSD of the output of M . (b) Shows the output y_k of S for all $k \in [0, 50]$. (c) Shows the output \hat{y}_k of M with $\hat{v} = 5.0736$ for all $k \in [0, 50]$. (d) Shows the output y_k of S for all $k \in [2500, 2510]$, and the output \hat{y}_k of M for all $k \in [2502, 2512]$.

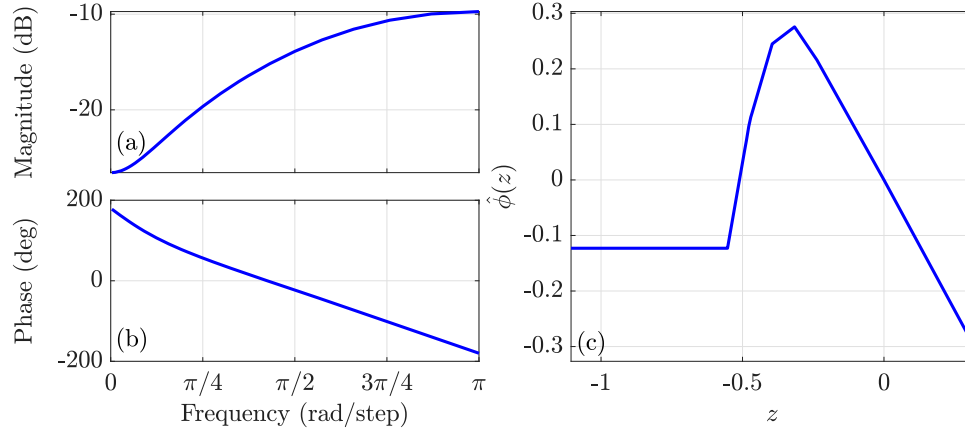


Figure 27. Example 8.1.3: MIO-ID of the logistic map equations (7)–(9) with $\gamma = 3.5$, using noiseless measurements. (a,b) Shows the frequency response \hat{G} . (c) shows the estimated nonlinearity $\hat{\phi}$.

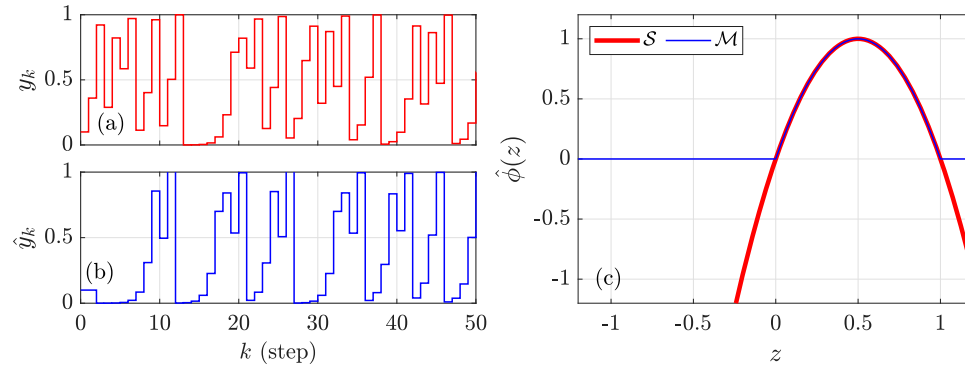


Figure 28. Example 8.1.4: Nonlinear identification of the logistic map equations (7)–(9) with $\gamma = 4$, using noiseless measurements. (a) Shows the output y_k of S for all $k \in [0, 50]$. (b) Shows the output \hat{y}_k of \mathcal{M} with $\hat{v} = 0$ for all $k \in [0, 50]$. (c) Shows the nonlinearity of the logistic map ϕ in (75) and the estimated nonlinearity $\hat{\phi}$ of \mathcal{M} .

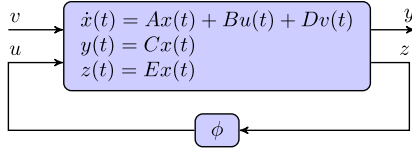


Figure 29. Continuous-time Lur'e system with input v , nonlinear feedback function ϕ , and output y .

where $n = p = 2$, $m = 1$, $x(t) = [x_1(t) \ x_2(t)]^T$, $y(t) = x_1(t)$, and $\gamma \in \mathbb{R}$.

Example 9.2: The dynamics of the Lotka-Volterra predator-prey system where the output is the number of prey can be written as

$$\dot{x}(t) = \begin{bmatrix} \alpha & 0 \\ 0 & -\gamma \end{bmatrix} x(t) + \begin{bmatrix} -\zeta \\ \xi \end{bmatrix} \phi(x(t)), \quad (85)$$

$$y(t) = [1 \ 0]x(t), \quad (86)$$

$$\phi(x(t)) = x_1(t)x_2(t), \quad (87)$$

where $n = p = 2$, $m = 1$, $x(t) = [x_1(t) \ x_2(t)]^T$, $y(t) = x_2(t)$, and $\alpha, \gamma, \zeta, \xi \in \mathbb{R}$.

10. Application to continuous-time numerical examples

In this section, we present examples to illustrate the application of MIO-ID to data obtained from numerical simulations from continuous-time systems. In these examples, since no true nonlinearity is available, the scaling parameter is chosen to be $\hat{\beta} = 1$. Furthermore, the phase portrait of the responses of both the continuous-time system S and the estimated model \mathcal{M} are displayed, in which an estimate of the output derivative is used, such that, for all $k > 1$,

$$\dot{y}_k \triangleq \frac{y_{k+1} - y_{k-1}}{2T_s}, \quad (88)$$

$$\dot{\hat{y}}_k \triangleq \frac{\hat{y}_{k+1} - \hat{y}_{k-1}}{2T_s}, \quad (89)$$

where T_s denotes the sampling time. Table 3 summarises the details of the considered continuous-time systems.

Table 3. Examples with continuous-time models.

Example	System type	System order	T_s (s)	SNR (dB)	Remark
10.1	van der Pol	2	0.1	∞ and 30	CTL system.
10.2	Lotka-Volterra				
10.3	Mackey-Glass	1			Time-delay system.

Example 10.1: van der Pol Oscillator

Let \mathcal{S} be the continuous-time van der Pol system, given by (82)–(84), where, for all $t \geq 0$, $\gamma = 1$, $x_1(0) = 0.1$, and $x_2(0) = 0$. To obtain data for identification, for all $t > 0$, the van der Pol model is simulated using ode45, and the output is sampled with sampling time $T_s = 0.1$ s. The integration accuracy of ode45 is set so that approximately 160 integration steps are implemented within each sample interval. For identification, we let $\hat{n} \in [1, 20]$, $\hat{d} \in [0, 25]$, $\hat{\lambda} \in [10, 1000]$, $\hat{v}_n \in [1, 15]$, and $\hat{v}_p \in [1, 15]$, with $l_l = l_{\text{MIO},l} = 500$, $l_u = 3000$, and $l_{\text{MIO},u} = 20,000$ that is, y_k for all $k \in [500, 3000]$ is used for least-squares optimisation, and y_k and \hat{y}_k for all $k \in [500, 20,000]$ is used to compute J_{MIO} .

Figure 30 compares the response of the model \mathcal{M} identified using MIO-ID in the presence of noiseless measurements with the response of \mathcal{S} . Figure 30 also compares the phase portraits

of the continuous-time system \mathcal{S} , and the identified model \mathcal{M} using (88) and (89) to approximate the derivative of the output. The estimated DTLL/CPA model parameters are $\hat{n} = 13$, $\hat{d} = 11$, $\hat{v}_n = 9$, $\hat{v}_p = 10$, $\hat{v} = -70.77 \cdot 10^{-4}$, \hat{G} with a frequency response shown in Figure 31, and $\hat{\phi}$ shown in Figure 31.

Next, consider the output of \mathcal{S} with sensor noise that yields an output signal with 30 dB SNR. Figure 32 compares the response of the model \mathcal{M} identified using MIO-ID in the presence of noisy measurements with the response of \mathcal{S} . Figure 32 also compares the phase portraits of the continuous-time system \mathcal{S} , with and without sensor noise, and the identified model \mathcal{M} using (88) and (89) to approximate the derivative of the output. The estimated DTLL/CPA model parameters are $\hat{n} = 47$, $\hat{d} = 7$, $\hat{v}_n = 16$, $\hat{v}_p = 10$, $\hat{v} = -0.4624$, \hat{G} with a frequency response shown in Figure 33, and $\hat{\phi}$ shown in Figure 33.

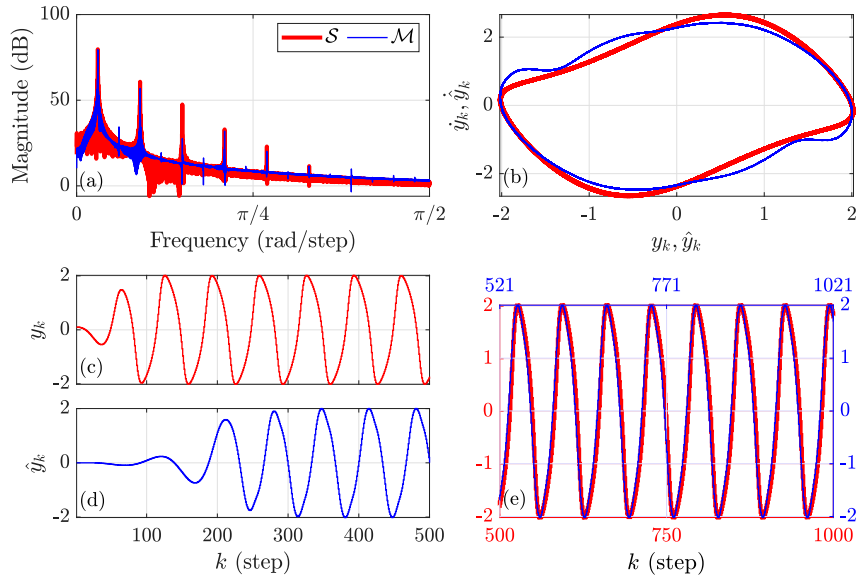


Figure 30. Example 10.1: MIO-ID of the continuous-time van der Pol oscillator using noiseless measurements. For the sampling time $T_s = 0.1$ s. (a) Compares the PSD of the output of \mathcal{S} with the PSD of the output of \mathcal{M} . (b) Shows the phase portraits of the response y of the continuous-time van der Pol system \mathcal{S} and the response \hat{y} of the identified model \mathcal{M} . The derivatives of the outputs are approximated using (88) and (89) with $T_s = 0.1$ s. (c) Shows the output y_k of \mathcal{S} for all $k \in [0, 500]$. (d) Shows the output \hat{y}_k of \mathcal{M} with $\hat{v} = -70.77 \cdot 10^{-4}$ for all $k \in [0, 500]$. (e) Shows the sampled output y_k of \mathcal{S} for all $k \in [500, 1000]$, and the output \hat{y}_k of \mathcal{M} for all $k \in [521, 1021]$.

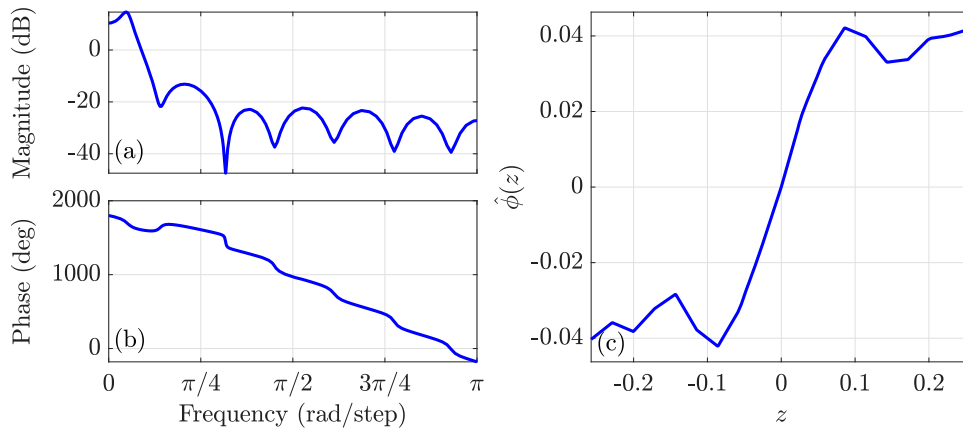


Figure 31. Example 10.1: MIO-ID of the continuous-time van der Pol oscillator using noiseless measurements. (a,b) Shows the frequency response of \hat{G} . (c) Shows the estimated nonlinearity $\hat{\phi}$ of \mathcal{M} .

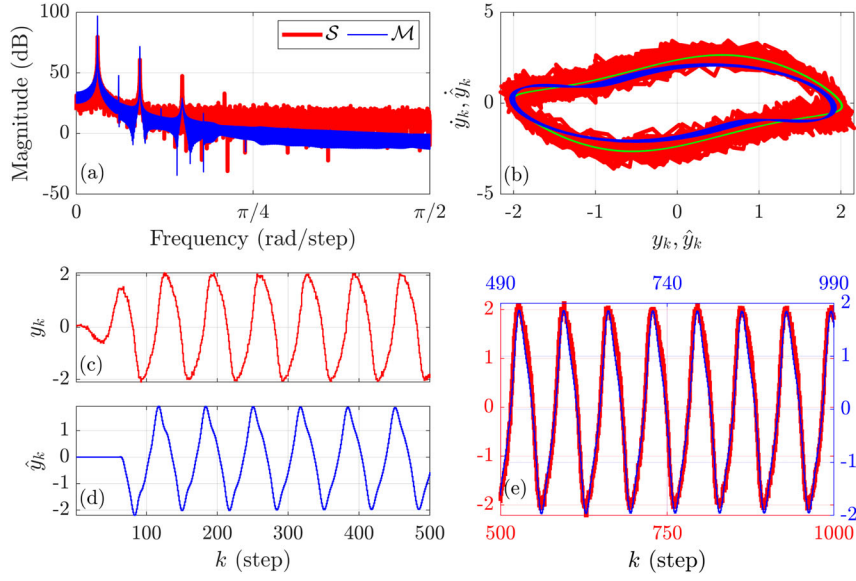


Figure 32. Example 10.1: MIO-ID of the continuous-time van der Pol oscillator with 30 dB SNR. For the sampling time $T_s = 0.1$ s. (a) Compares the PSD of the output of \mathcal{S} with the PSD of the output of \mathcal{M} . (b) Shows the phase portraits of the response y of the continuous-time van der Pol system \mathcal{S} with sensor noise, response of the continuous-time van der Pol system \mathcal{S} without sensor noise in green, and the response \hat{y} of the identified model \mathcal{M} . The derivatives of the outputs are approximated using (88) and (89) with $T_s = 0.1$ s. (c) Shows the output y_k of \mathcal{S} for all $k \in [0, 500]$. (d) Shows the output \hat{y}_k of \mathcal{M} with $\hat{v} = 0.6444$ for all $k \in [0, 500]$. (e) Shows the sampled output y_k of \mathcal{S} for all $k \in [500, 1000]$, and the output \hat{y}_k of \mathcal{M} for all $k \in [490, 990]$.

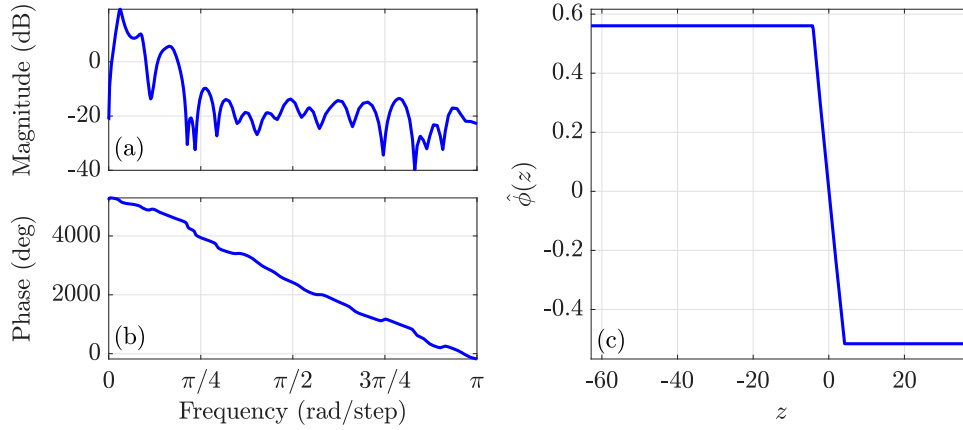


Figure 33. Example 10.1: MIO-ID of the continuous-time van der Pol oscillator with 30 dB SNR. (a,b) Shows the frequency response of \hat{G} . (c) Shows the estimated nonlinearity $\hat{\phi}$.

Example 10.2: Lotka-Volterra Model

Let \mathcal{S} be the continuous-time Lotka-Volterra model, given by (85)–(87) where, for all $t \geq 0$, $\alpha = 2/3$, $\gamma = 1$, $\zeta = 4/3$, $\xi = 1$, and $x(0) = y(0) = 1$. To obtain data for identification, for all $t > 0$, the Lotka-Volterra model is simulated using ode45, and the output is sampled with sampling time $T_s = 0.1$ s. The integration accuracy of ode45 is set so that approximately 160 integration steps are implemented within each sample interval. For identification, we let $\hat{n} \in [1, 30]$, $\hat{d} \in [0, 30]$, $\hat{\lambda} \in [10, 5000]$, $\hat{v}_n \in [1, 10]$, and $\hat{v}_p \in [1, 10]$, with $l_l = l_{M,l} = 100$ and $l_u = l_{M,u} = 10,000$, that is, y_k for all $k \in [100, 10,000]$ is used for identification. Figure 34 compares the response of the model \mathcal{M} , identified using MIO-ID, with the response of \mathcal{S} . Figure 34 also

compares the phase portraits of the continuous-time system \mathcal{S} and the identified model \mathcal{M} using (88) and (89) to approximate the derivative of the output. The estimated DTLI/CPA model parameters are $\hat{n} = 14$, $\hat{d} = 16$, $\hat{v}_n = 7$, $\hat{v}_p = 7$, $\hat{v} = 0.258$, \hat{G} with a frequency response shown in Figure 35, and $\hat{\phi}$ shown in Figure 35.

Next, consider the output of \mathcal{S} with sensor noise that yields an output signal with 30 dB SNR. Figure 36 compares the response of the model \mathcal{M} identified using MIO-ID in the presence of noisy measurements with the response of \mathcal{S} . Figure 36 also compares the phase portraits of the continuous-time system \mathcal{S} , with and without sensor noise, and the identified model \mathcal{M} using (88) and (89) to approximate the derivative of the output.

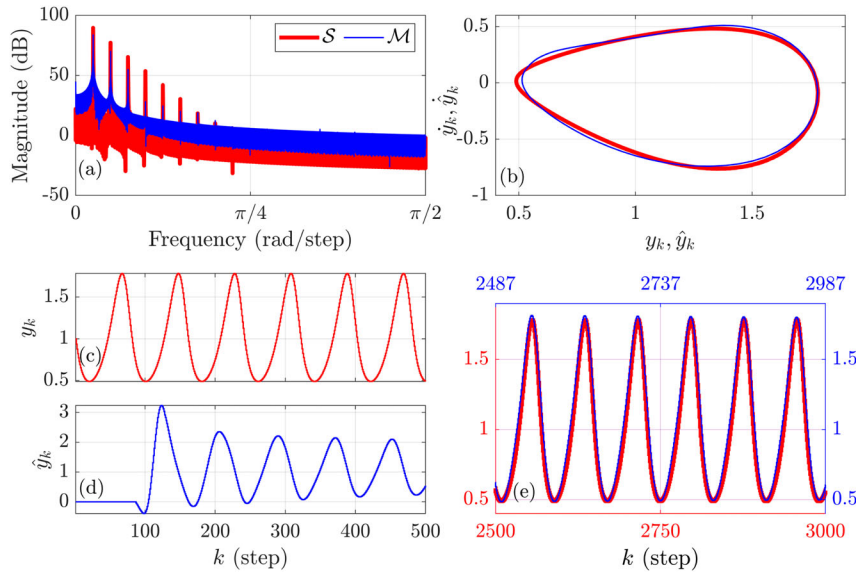


Figure 34. Example 10.2: MIO-ID of the continuous-time Lotka-Volterra model using noiseless measurements. (a) Compares the PSD of the output of \mathcal{S} with sampling time $T_s = 0.1$ s, with the PSD of the output of \mathcal{M} . (b) Shows the phase portraits of the response y of the continuous-time van der Pol system \mathcal{S} and the response \hat{y} of the identified model \mathcal{M} . The derivatives of the outputs are approximated using (88) and (89) with $T_s = 0.1$ s. (c) Shows the output y_k of \mathcal{S} for all $k \in [0, 500]$. (d) Shows the output \hat{y}_k of \mathcal{M} with $\hat{v} = 0.258$ for all $k \in [0, 500]$. (e) Shows the sampled output y_k of \mathcal{S} for all $k \in [2500, 3000]$, and the output \hat{y}_k of \mathcal{M} for all $k \in [2487, 2987]$.

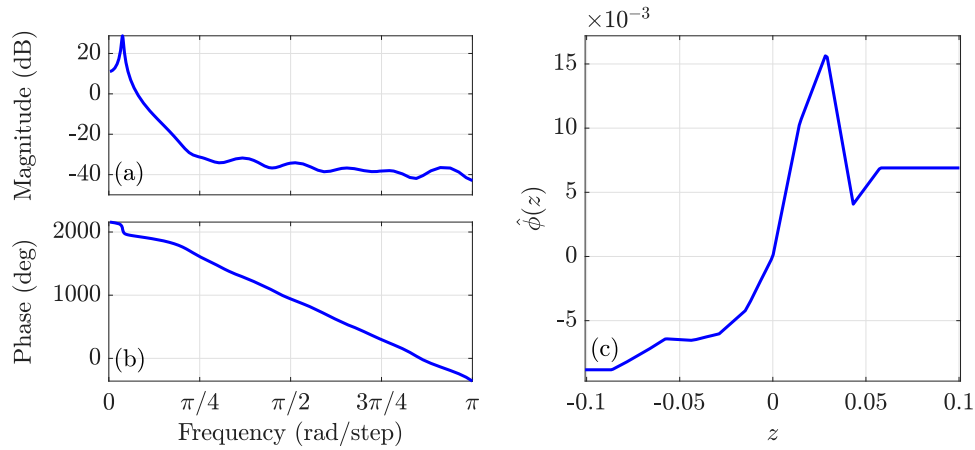


Figure 35. Example 10.2: MIO-ID of the continuous-time Lotka-Volterra model using noiseless measurements. (a,b) Shows the frequency response of \hat{G} . (c) Shows the estimated nonlinearity $\hat{\phi}$.

The estimated DTLI/CPA model parameters are $\hat{n} = 48$, $\hat{d} = 25$, $\hat{v}_n = 7$, $\hat{v}_p = 12$, $\hat{v} = -3.3042$, \hat{G} with a frequency response shown in Figure 37, and $\hat{\phi}$ shown in Figure 37.

Example 10.3: Mackey-Glass Model

Let \mathcal{S} be the continuous-time, time-delayed Mackey-Glass model, given by the delay differential equation

$$\dot{x}(t) = -\gamma x(t) + \frac{\zeta x(t - \tau)}{1 + x^\xi(t - \tau)}, \quad (90)$$

$$y(t) = x(t), \quad (91)$$

where $\gamma = 0.1$, $\zeta = 0.2$, $\tau = 6$, $\xi = 10$, and, for all $t \leq 0$, $x(t) = 0.1$. Note that this system cannot be represented by the structure proposed in Section 9. This example illustrates that MIO-ID is

able to identify systems with continuous-time delay. To obtain data for identification, for all $t > 0$, the Mackey Glass equation is simulated using dde23, and the output is sampled with sampling time $T_s = 0.1$ s. The integration accuracy of dde23 is set so that approximately 160 integration steps are implemented within each sample interval. For identification, we let $\hat{n} \in [1, 50]$, $\hat{d} \in [0, 50]$, $\hat{\lambda} \in [1, 50,000]$, $\hat{v}_n \in [1, 20]$, and $\hat{v}_p \in [1, 20]$, with $l_1 = l_{\text{MIO},l} = 1000$, $l_u = 3000$, and $l_{\text{MIO},u} = 20,000$, that is, y_k for all $k \in [1000, 3000]$ is used for least-squares optimisation, and y_k and \hat{y}_k for all $k \in [1000, 20,000]$ is used to compute J_{MIO} . Figure 38 compares the response of the model \mathcal{M} identified using MIO-ID with the response of \mathcal{S} . Figure 38 also compares the phase portraits of the continuous-time system \mathcal{S} and the identified model \mathcal{M} using (88) and (89) to approximate the derivative of the output. The estimated DTLI/CPA model parameters are $\hat{n} = 44$, $\hat{d} = 13$, $\hat{v}_n = 9$, $\hat{v}_p = 14$, $\hat{v} = 25.965$, \hat{G}

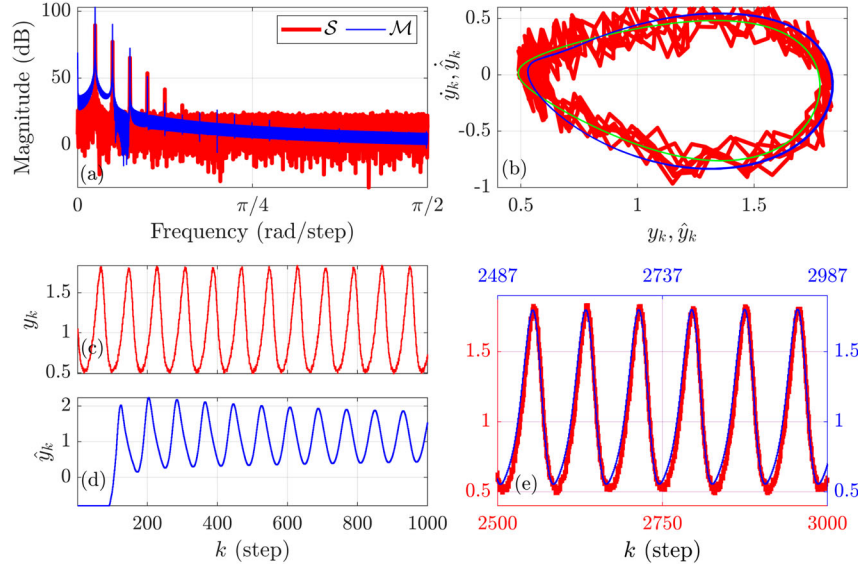


Figure 36. Example 10.2: MIO-ID of the continuous-time Lotka-Volterra model with 30 dB SNR. (a) Compares the PSD of the output of \mathcal{S} with sampling time $T_s = 0.1$ s, with the PSD of the output of \mathcal{M} . (b) Shows the phase portraits of the response y of the continuous-time van der Pol system \mathcal{S} with sensor noise, response of the continuous-time Lotka-Volterra model \mathcal{S} without sensor noise in green, and the response \hat{y} of the identified model \mathcal{M} . The derivatives of the outputs are approximated using (88) and (89) with $T_s = 0.1$ s. (c) Shows the output y_k of \mathcal{S} for all $k \in [0, 500]$. (d) Shows the output \hat{y}_k of \mathcal{M} with $\hat{\nu} = 0.258$ for all $k \in [0, 500]$. (e) Shows the sampled output y_k of \mathcal{S} for all $k \in [2500, 3000]$, and the output \hat{y}_k of \mathcal{M} for all $k \in [2487, 2987]$.

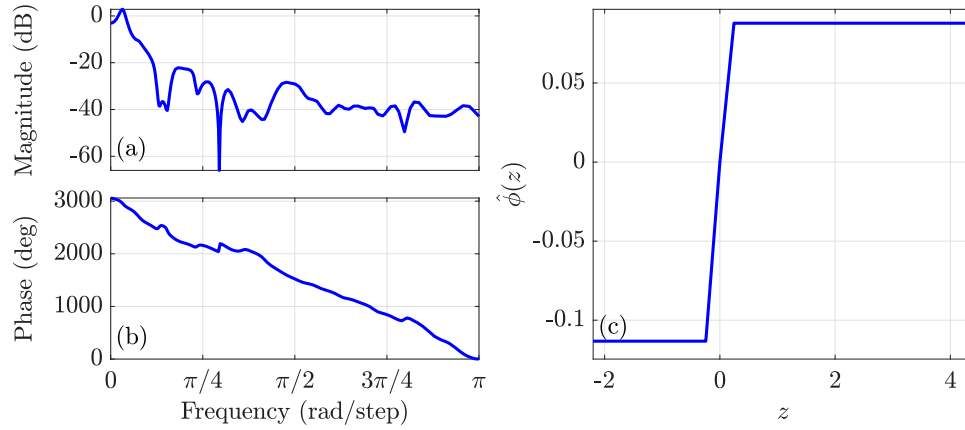


Figure 37. Example 10.2: MIO-ID of the continuous-time Lotka-Volterra model with 30 dB SNR. (a,b) Shows the frequency response of \hat{G} . (c) Shows the estimated nonlinearity $\hat{\phi}$.

with a frequency response shown in Figure 39, and $\hat{\phi}$ shown in Figure 39.

Next, consider the output of \mathcal{S} with sensor noise that yields an output signal with 30 dB SNR. Figure 40 compares the response of the model \mathcal{M} identified using MIO-ID in the presence of noisy measurements with the response of \mathcal{S} . Figure 40 also compares the phase portraits of the continuous-time system \mathcal{S} , with and without sensor noise, and the identified model \mathcal{M} using (88) and (89) to approximate the derivative of the output. The estimated DTLI/CPA model parameters are $\hat{n} = 50$, $\hat{a} = 48$, $\hat{\nu}_n = 15$, $\hat{\nu}_p = 14$, $\hat{\nu} = 0.1604$, \hat{G} with a frequency response shown in Figure 41, and $\hat{\phi}$ shown in Figure 41.

11. Application to experimental data

In this section, we present examples to illustrate the application of MIO-ID to data obtained via experiments from sensor data sets and show that MIO-ID may be used to identify a wide range of systems that exhibit oscillatory behaviour. In these examples, since no true nonlinearity is available, the scaling parameter is chosen to be $\hat{\beta} = 1$. Furthermore, the phase portrait of the responses of both the system \mathcal{S} and the estimated model \mathcal{M} are displayed, in which the estimate of the output derivative shown in (88) and (89) is used. Table 4 summarises the details of the experimental data sets considered, where $f_s \triangleq 1/T_s$ denotes the sampling rate in Hz.

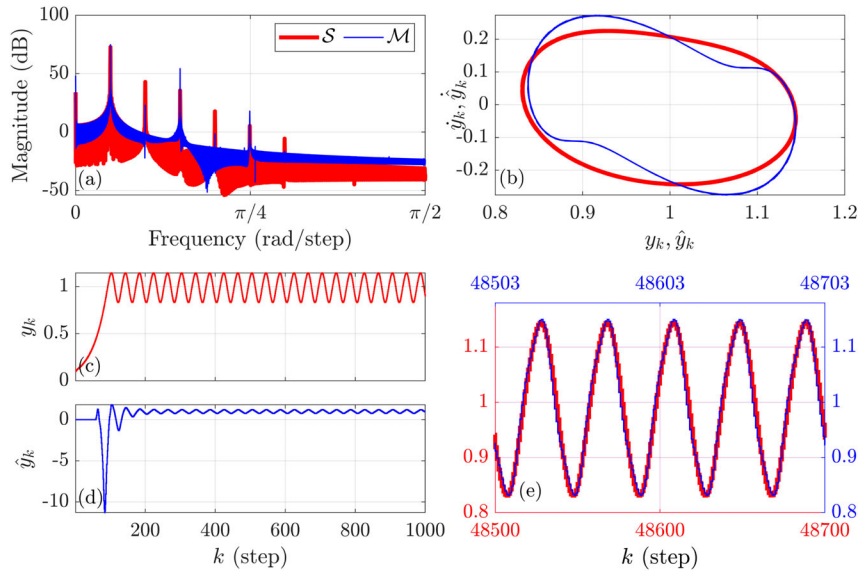


Figure 38. Example 10.3: MIO-ID of the continuous-time Mackey-Glass model using noiseless measurements. (a) Compares the PSD of the output of S with sampling time $T_s = 0.1$ s, with the PSD of the output of \mathcal{M} . (b) Shows the phase portraits of the response y of the continuous-time van der Pol system S and the response \hat{y} of the identified model \mathcal{M} . The derivatives of the outputs are approximated using (88) and (89) with $T_s = 0.1$ s. (c) Shows the output y_k of S for all $k \in [0, 1000]$. (d) Shows the output \hat{y}_k of \mathcal{M} with $\hat{v} = 25.965$ for all $k \in [0, 1000]$. (e) Shows the sampled output y_k of S for all $k \in [48,500, 48,700]$, and the output \hat{y}_k of \mathcal{M} for all $k \in [48,503, 48,703]$.

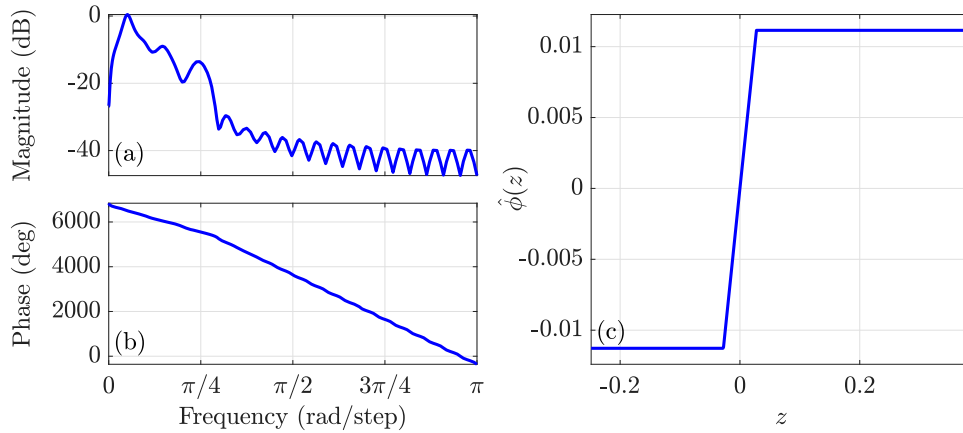


Figure 39. Example 10.3: MIO-ID of the continuous-time Mackey-Glass model using noiseless measurements. (a,b) Show the frequency response of \hat{G} . (c) Shows the estimated nonlinearity $\hat{\phi}$.

Example 11.1: Experimental data from flute (A4 note)

In this example, the experimental data obtained from the recording of an A4 note from a flute used in Petersen (2004) is used for identification. Let S be the flute and consider a sampling rate of $f_s = 22,050$ Hz. For identification, we let $\hat{n} \in [1, 150]$, $\hat{d} \in [0, 150]$, $\hat{\lambda} \in [1, 50,000]$, $\hat{v}_n \in [1, 30]$, and $\hat{v}_p \in [1, 30]$, with $l_l = l_{\text{MIO},l} = 500$, $l_u = 2500$, and $l_{\text{MIO},u} = 50,000$ that is, y_k for all $k \in [500, 2500]$ is used for least-squares optimisation, and y_k and \hat{y}_k for all $k \in [500, 50,000]$ is used to compute J_{MIO} . Since the flute was played by a human, the recorded waveform shows significant variation as time increases, which is why a consistent subset of the data during the beginning of the recording (between 0.3810 s and 0.6122 s) was chosen for identification. Figure 42 compares the response of the model identified using MIO-ID with the measurements obtained from the flute. Figure 42 also compares the phase portraits of the flute

data (system S) and the identified model \mathcal{M} using (88) and (89) to approximate the derivative of the output with $T_s = 1/f_s$ s. The estimated DTLI/CPA model parameters are $\hat{n} = 87$, $\hat{d} = 29$, $\hat{v}_n = 25$, $\hat{v}_p = 24$, $\hat{v} = 0.7513$, \hat{G} with a frequency response shown in Figure 43, and $\hat{\phi}$ shown in Figure 43.

Example 11.2: Experimental data from gas-turbine combustor (thermoacoustic oscillations)

In this example, experimental data obtained from a recording of the sound generated by thermoacoustic oscillations during the operation of a gas-turbine combustor is used for identification. Let S be the Dual Independent Swirl Combustor Facility (DISCo), featured in Ramesh et al. (2021). This model combustor was designed to exhibit thermoacoustic instabilities, which are typically generated by the coupling of the unsteady

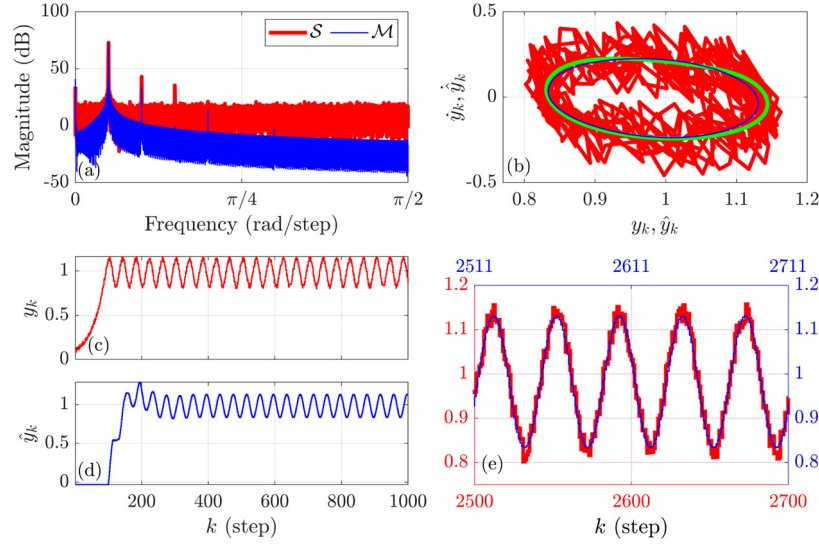


Figure 40. Example 10.3: MIO-ID of the continuous-time Mackey-Glass model with 30 dB SNR. (a) Compares the PSD of the output of \mathcal{S} with sampling time $T_s = 0.1$ s, with the PSD of the output of \mathcal{M} . (b) Shows the phase portraits of the response y of the continuous-time van der Pol system \mathcal{S} , response of the continuous-time van der Pol system \mathcal{S} without sensor noise in green, and the response \hat{y} of the identified model \mathcal{M} . The derivatives of the outputs are approximated using (88) and (89) with $T_s = 0.1$ s. (c) Shows the output y_k of \mathcal{S} for all $k \in [0, 1000]$. (d) Shows the output \hat{y}_k of \mathcal{M} with $\hat{\nu} = 25.965$ for all $k \in [0, 1000]$. (e) Shows the sampled output y_k of \mathcal{S} for all $k \in [48,500, 48,700]$, and the output \hat{y}_k of \mathcal{M} for all $k \in [48,503, 48,703]$.

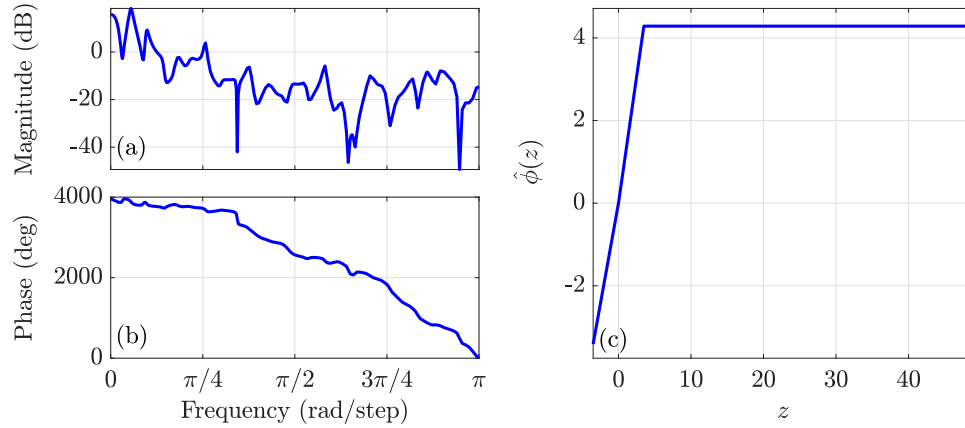


Figure 41. Example 10.3: MIO-ID of the continuous-time Mackey-Glass model with 30 dB SNR. (a,b) Shows the frequency response of \hat{G} . (c) Shows the estimated nonlinearity $\hat{\phi}$.

Table 4. Examples with experimental data.

Example	System type	f_s (Hz)
11.1	Flute A4 Note	22,050
11.2	Gas-Turbine Combustor	15,000

combustion process with the acoustic properties of the combustion chamber and air/fuel plenums. The commissioned DISCo facility is shown in Figure 44. The combustor allows for the independent manipulation of the mass flow rate through each of a total of five flowpaths: fuel (\dot{m}_f), primary air outer swirler (\dot{m}_{so}), primary air inner swirler (\dot{m}_{si}), secondary air outer axial swirler (\dot{m}_{ao}) and secondary air inner axial swirler (\dot{m}_{ai}) lines. The data used for identification was obtained from a microphone (Kulite type MIC-190L) placed in the combustion chamber, as is shown in Figure 44, with a sensitivity of 9 Pa/mV,

computed after the signal is amplified. The pressure measurements from this sensor were acquired at a sampling rate of $f_s = 15,000$ Hz.

Consider a run of the DISCo system where the mass flow rates of the flowpaths are kept constant, such that $\dot{m}_f \equiv 0.52$ g/s, $\dot{m}_{so} \equiv 3.84$ g/s, $\dot{m}_{si} \equiv 6.16$ g/s, $\dot{m}_{ao} \equiv 0$ g/s, and $\dot{m}_{ai} \equiv 0$ g/s. The microphone measurements show that, after some time, the pressure fluctuations display oscillatory behaviour, as is shown in Figure 45.

For identification, we let $\hat{n} \in [1, 75]$, $\hat{d} \in [0, 75]$, $\hat{\lambda} \in [1, 20,000]$, $\hat{\nu}_n \in [1, 30]$, and $\hat{\nu}_p \in [1, 30]$, with $l_l = 2505$, $l_u = 2685$, $l_{MIO,l} = 1000$, and $l_{MIO,u} = 60,000$ that is, y_k for all $k \in [2505, 2685]$ is used for least-squares optimisation, and y_k and \hat{y}_k for all $k \in [1000, 60,000]$ is used to compute J_{MIO} . This arrangement was chosen due to the irregularity of the oscillatory behaviour displayed by the data. A representative waveform from the available data is chosen to minimise J , and this

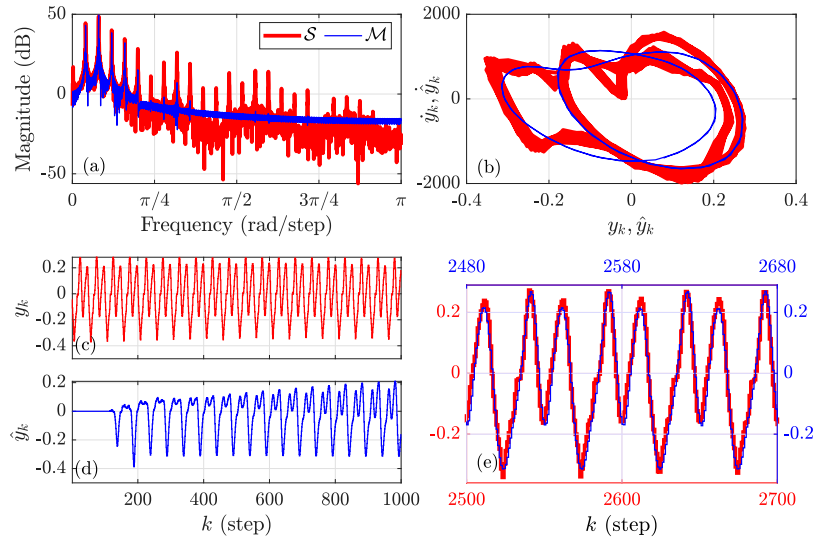


Figure 42. Example 11.1: MIO-ID using the data from a recording of a flute (A4 note). (a) Compares the PSD of the sampled output of S with the PSD of the output of M . (b) Shows the estimated phase portraits of the response y of S and the response \hat{y} of the identified model M . The derivatives of the outputs of S and M are approximated by using (88) and (89) with $T_s = 1/f_s$ s and $f_s = 22,050$ Hz. (c) Shows the output y_k of S for all $k \in [0, 1000]$. (d) Shows the output \hat{y}_k of M with $\hat{\nu} = 0.7513$ for all $k \in [0, 1000]$. (e) Shows the output y_k of S for all $k \in [2500, 2700]$, and the output \hat{y}_k of M for all $k \in [2480, 2780]$.

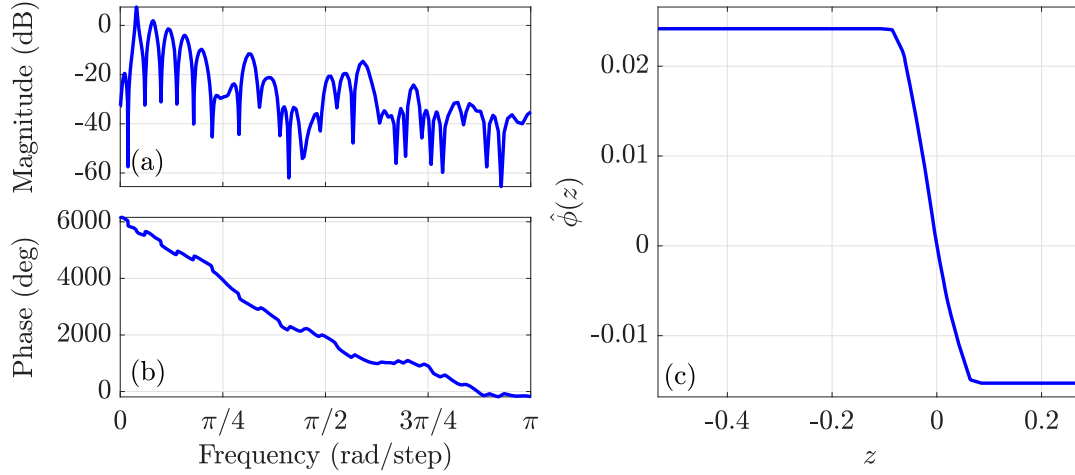


Figure 43. Example 11.1: MIO-ID using the data from a recording of a flute (A4 note). (a,b) Shows the frequency response of \hat{G} . (c) Shows the estimated nonlinearity $\hat{\phi}$.

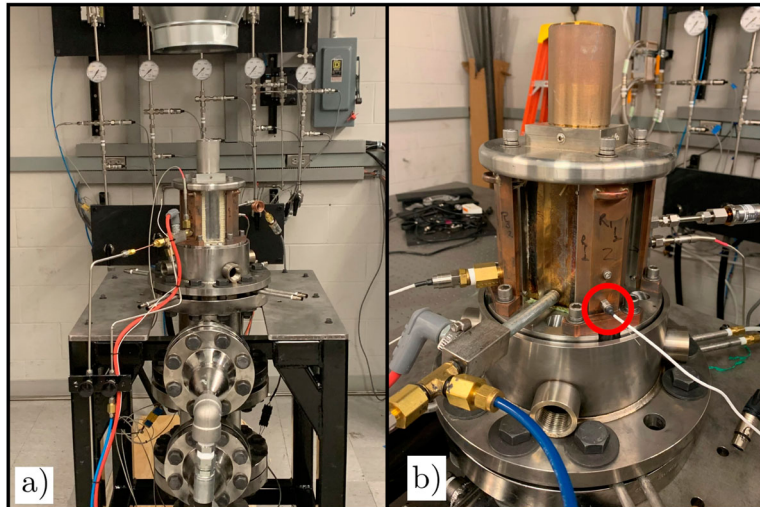


Figure 44. Example 11.2: DISCo facility. (a) Commissioned DISCo facility in atmospheric condition. (b) Placement of microphone in the combustion chamber used for pressure data recording.

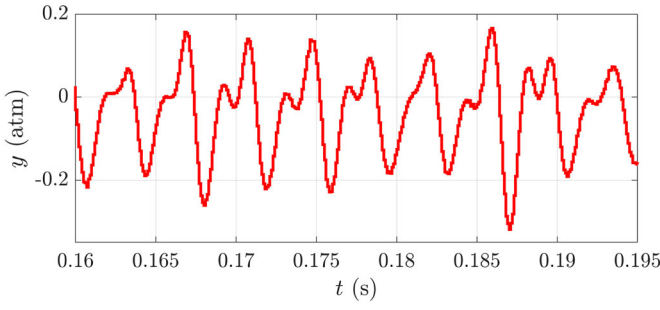


Figure 45. Example 11.2: Original signal from DISCo combustor

waveform is used to determine the accuracy of the identified model.

Figure 46 compares the response of the model identified using MIO-ID with the measurements obtained from the combustor. Furthermore, Figure 46 compares the phase portraits of the combustor data (system \mathcal{S}) and the identified model \mathcal{M}

using (88) and (89) to approximate the derivative of the output with $T_s = 1/f_s$ s. The estimated DTLI/CPA model parameters are $\hat{n} = 59$, $\hat{d} = 26$, $\hat{v}_n = 9$, $\hat{v}_p = 8$, $\hat{v} = 0.7765$, the frequency response of \hat{G} is shown in Figure 47, and $\hat{\phi}$ is shown in Figure 47.

12. Conclusions

This paper presented a framework for identifying SES's based on a DTL model. The nonlinear feedback function was chosen to be CPA parameterised by its slope in each interval of a partition of the real line. A mixed-integer optimisation approach was used for parameter estimation within the DTLI model as an extension of the technique presented in Paredes and Bernstein (2021). This approach allows optimisation of the model parameters that were previously chosen manually, thus improving the identification accuracy and reducing the effort required by the user. Numerical examples included both discrete-time and continuous-time systems with noiseless and noisy sampled data.

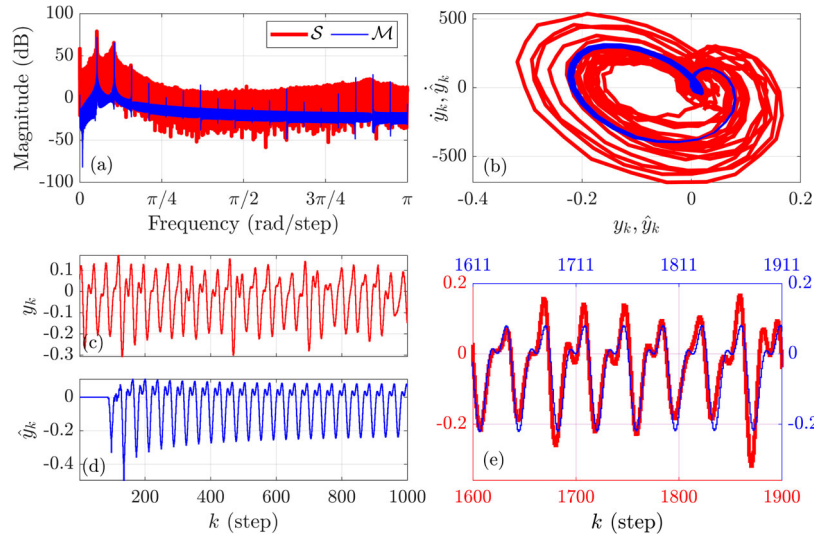


Figure 46. Example 11.2: MIO-ID using the data from a recording of sound generated by thermoacoustic oscillations during the operation of a gas-turbine combustor. (a) Compares the PSD of the sampled output of \mathcal{S} with the PSD of the output of \mathcal{M} . (b) Shows the estimated phase portraits of the response y of \mathcal{S} and the response \hat{y} of the identified model \mathcal{M} . The derivatives of the outputs of \mathcal{S} and \mathcal{M} are approximated using (88) and (89) with $T_s = 1/f_s$ s and $f_s = 15,000$ Hz. (c) Shows the output y_k of \mathcal{S} for all $k \in [0, 1000]$. (d) Shows the output \hat{y}_k of \mathcal{M} with $\hat{v} = 0.7765$ for all $k \in [0, 1000]$. (e) Shows the output y_k of \mathcal{S} for all $k \in [1600, 1900]$, and the output \hat{y}_k of \mathcal{M} for all $k \in [1611, 1911]$.

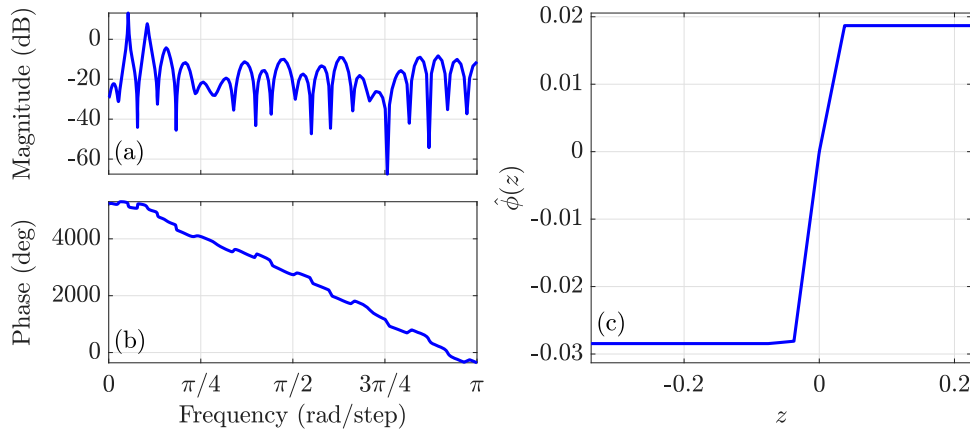


Figure 47. Example 11.2: MIO-ID using the data from a recording of sound generated by thermoacoustic oscillations during the operation of a gas-turbine combustor. (a,b) Shows the frequency response of linear dynamics \hat{G} of \mathcal{M} . (c) Shows the estimated nonlinearity $\hat{\phi}$ of \mathcal{M} .

Finally, the MIO-ID was applied to a data set obtained from a gas-turbine combustor, which resulted in a DTLI model that closely reproduced the oscillatory behaviour displayed by the combustor. Although the combustor does not have the structure of a DTL model, the system identification technique was able to approximately reproduce the phase-plane dynamics of these systems. Future research will focus on adapting this approach to the case where the nonlinearity is a hysteresis.

Disclosure statement

No potential conflict of interest was reported by the author(s).

Funding

This research was supported by the NSF grant CMMI 1634709.

ORCID

Juan A. Paredes  <http://orcid.org/0000-0001-7486-1231>

Dennis S. Bernstein  <http://orcid.org/0000-0003-0399-3039>

References

- Aguilar, L. T., Boiko, I., Fridman, L., & Iriarte, R. (2009). Generating self-excited oscillations via two-relay controller. *IEEE Transactions on Automatic Control*, 54(2), 416–420. <https://doi.org/10.1109/TAC.2008.2009615>
- Aström, K. J., & Wittenmark, B. (1995). *Adaptive Control* (2nd ed.). Addison-Wesley.
- Belotti, P., Kirches, C., Leyffer, S., Linderoth, J., Luedtke, J., & Mahajan, A. (2013). Mixed-integer nonlinear optimization. *Acta Numerica*, 22, 1–131. <https://doi.org/10.1017/S0962492913000032>
- Bernstein, D. S. (2018). *Scalar, Vector, and Matrix Mathematics: Theory, Facts, and Formulas* (Expanded Ed.). Princeton University Press.
- Blevins, R. D. (1990). *Flow-Induced Vibration*. Van Nostrand Reinhold.
- Chatterjee, S. (2011). Self-excited oscillation under nonlinear feedback with time-delay. *Journal of Sound and Vibration*, 330(9), 1860–1876. <https://doi.org/10.1016/j.jsv.2010.11.005>
- Chen, Y., & Driscoll, J. F. (2016). A multi-chamber model of combustion instabilities and its assessment using kilohertz laser diagnostics in a gas turbine model combustor. *Combustion and Flame*, 174, 120–137. <https://doi.org/10.1016/j.combustflame.2016.08.022>
- D'Amico, M. B., Moiola, J. L., & Paolini, E. E. (2002). Hopf bifurcation for maps: A frequency-domain approach. *IEEE Transactions on Circuits and Systems I: Fundamental Theory and Applications*, 49(3), 281–288. <https://doi.org/10.1109/81.989161>
- Ding, W. (2010). *Self-Excited Vibration: Theory, Paradigms, and Research Methods*. Springer.
- Dowling, A. P. (1997). Nonlinear self-excited oscillations of a ducted flame. *Journal of Fluid Mechanics*, 346, 271–291. <https://doi.org/10.1017/S0022112097006484>
- Dua, V. (2010). A mixed-integer programming approach for optimal configuration of artificial neural networks. *Chemical Engineering Research & Design*, 88(1), 55–60. <https://doi.org/10.1016/j.cherd.2009.06.007>
- Floudas, C. (1995). *Nonlinear and Mixed-Integer Optimization*. Oxford University Press.
- Förster, D., Inderka, R. B., & Gauterin, F. (2019). Data-driven identification of characteristic real-driving cycles based on k-means clustering and mixed-integer optimization. *IEEE Transactions on Vehicular Technology*, 69(3), 2398–2410. <https://doi.org/10.1109/TVT.2019.2939125>
- Gentile, F. S., Bel, A. L., D'Amico, M. B., & Moiola, J. L. (2011). Effect of delayed feedback on the dynamics of a scalar map via a frequency-domain approach. *Chaos*, 21(2), 023117. <https://doi.org/10.1063/1.3595707>
- Gianikos, Z., Kirschmeier, B., Gopalathnam, A., & Bryant, M. (2020). Limit cycle characterization of an aeroelastic wing in a bluff body wake. *Journal of Fluids and Structures*, 95, 102986. <https://doi.org/10.1016/j.jfluidstructs.2020.102986>
- Goldbeter, A., & Berridge, M. J. (1996). *Biochemical oscillations and cellular rhythms: The molecular bases of periodic and chaotic behaviour*. Cambridge University Press.
- Gray, P., & Scott, S. K. (1990). *Chemical Oscillations and Instabilities: Non-linear Chemical Kinetics*. Clarendon Press.
- Guckenheimer, J., Oster, G., & Ipaktchi, A. (1977). The dynamics of density dependent population models. *Journal of Mathematical Biology*, 4(2), 101–147. <https://doi.org/10.1007/BF00275980>
- Jenkins, A. (2013). Self-oscillation. *Physics Reports*, 525(2), 167–222. <https://doi.org/10.1016/j.physrep.2012.10.007>
- Jonsson, E., Riso, C., Lupp, C. A., Cesnik, C. E. S., Martins, J. R. R. A., & Epureanu, B. I. (2019). Flutter and post-flutter constraints in aircraft design optimization. *Progress in Aerospace Sciences*, 109, 100537. <https://doi.org/10.1016/j.paerosci.2019.04.001>
- Khalil, H. K. (2002). *Nonlinear Systems* (3rd ed.). Prentice Hall.
- Mees, A., & Chua, L. (1979). The Hopf bifurcation theorem and its applications to nonlinear oscillations in circuits and systems. *IEEE Transactions on Circuits and Systems*, 26(4), 235–254. <https://doi.org/10.1109/TCS.1979.1084636>
- Mejari, M., Naik, V. V., Piga, D., & Bemporad, A. (2020). Identification of hybrid and linear parameter-varying models via piecewise affine regression using mixed integer programming. *International Journal of Robust and Nonlinear Control*, 30(15), 5802–5819. <https://doi.org/10.1002/rnc.v30.15>
- Paredes, J., & Bernstein, D. S. (2020). Identification of self-excited systems using discrete-time, time-delayed Lur'e models. arXiv:2004.14488.
- Paredes, J., & Bernstein, D. S. (2021). *Identification of self-excited systems using discrete-time, time-delayed Lur'e models*. 2021 American Control Conference. (pp. 3939–3944).
- Paredes, J., Islam, S. A. U., & Bernstein, D. S. (2020). A time-delayed Lur'e model with biased self-excited oscillations. 2020 American Control Conference. (pp. 2699–2704)
- Paredes, J., Islam, S. A. U., Kouba, O., & Bernstein, D. S. (2021). Self-excited dynamics of discrete-time Lur'e systems. arXiv:2109.12732.
- Petersen, M. R. (2004). Musical analysis and synthesis in MATLAB. *The College Mathematics Journal*, 35(5), 396–401. <https://doi.org/10.2307/4146853>
- Ramesh, R., Obidov, S., Paredes, J., Bernstein, D. S., & Gamba, M. (2021). *Design and characterization of the dual independent swirl combustor facility (DISCO)*. AIAA Propulsion and Energy 2021 Forum, (p. 3479) <https://doi.org/10.2514/6.2021-3479>
- Rasvan, V. (1998). *Self-sustained oscillations in discrete-time nonlinear feedback systems*. 1998 Mediterranean Electrotechnical Conference. (pp. 563–565)
- Risau-Gusman, S. (2016). Effects of time-delayed feedback on the properties of self-sustained oscillators. *Physical Review E*, 94(4), 042212. <https://doi.org/10.1103/PhysRevE.94.042212>
- Roll, J., Bemporad, A., & Ljung, L. (2004). Identification of piecewise affine systems via mixed-integer programming. *Automatica*, 40(1), 37–50. <https://doi.org/10.1016/j.automatica.2003.08.006>
- Stan, G., & Sepulchre, R. (2007). Analysis of interconnected oscillators by dissipativity theory. *IEEE Transactions on Automatic Control*, 52(2), 256–270. <https://doi.org/10.1109/TAC.2006.890471>
- Van Pelt, T. H., & Bernstein, D. S. (2001). Non-linear system identification using Hammerstein and non-linear feedback models with piecewise linear static maps. *International Journal of Control*, 74(18), 1807–1823. <https://doi.org/10.1080/00207170110089798>
- Zanette, D. H. (2017). Self-sustained oscillations with delayed velocity feedback. *Papers in Physics*, 9(1), 090003-1–090003-7. <https://doi.org/10.4279/pip.090003>